

# We are IntechOpen, the world's leading publisher of Open Access books Built by scientists, for scientists

6,000

Open access books available

148,000

International authors and editors

185M

Downloads

Our authors are among the

154

Countries delivered to

TOP 1%

most cited scientists

12.2%

Contributors from top 500 universities



WEB OF SCIENCE™

Selection of our books indexed in the Book Citation Index  
in Web of Science™ Core Collection (BKCI)

Interested in publishing with us?  
Contact [book.department@intechopen.com](mailto:book.department@intechopen.com)

Numbers displayed above are based on latest data collected.  
For more information visit [www.intechopen.com](http://www.intechopen.com)



Chapter

# Correlations in Scattered Phase Singular Beams

*Patnala Vanitha, Gangi Reddy Salla and Ravindra Pratap Singh*

## Abstract

We discuss about the correlations present in the scattered phase singular beams and utilize them for obtaining the corresponding mode information. We experimentally generate the coherence vortices using the cross-correlation functions between the speckle patterns and validate them with the exact analytical expressions. We also explore their propagation characteristics by considering their geometry along with their divergence. We utilize the autocorrelation measurements of speckle patterns for obtaining the mode information. Further, we study the correlations present in scattered perfect optical vortices which lead to a new class of coherence functions, Bessel-Gauss coherence functions, and utilized for generating the non-diffracting random fields, i.e. propagation invariant fields. We utilized these correlation functions, which are order-dependent although the speckle patterns are order-independent, for encrypting the information which has higher advantage than normal random optical fields.

**Keywords:** phase singular beams, scattering, speckles, correlation function, optical encryption

## 1. Introduction

Phase singular beams or optical vortices are well known due to their applications in guiding the particles, for coding larger information per photon, for transferring spatial structure to the materials, and for enhanced accuracy in metrological measurements [1–10]. These beams have ring-shaped intensity distribution along with helical wavefronts and have phase singularity at the center [11–16]. These beams carry an orbital angular momentum (OAM) of  $m\hbar$  per photon due to its azimuthal phase, where  $m$  is the order or topological charge defined as number of helices completed in one wavelength. The propagation of these light beams through various media such as turbid media [17, 18], turbulence atmosphere [19, 20], and under water [21, 22] have attracted lot of interest in recent days for utilizing them for communication applications [23–30]. The vortices can be generated using computer generated holography [31, 32] along with the help of spatial light modulator [33, 34], spiral phase plate [35, 36], and using an astigmatic mode converter [37]. Some advanced techniques have been introduced for generating vortex beams through laser cavity and using materials [38, 39]. After including the polarization to the spatial mode of light beam,

we get the vector vortices which have been studied extensively for sensing and communication applications [40, 41]. For sensing the magnetic field, these beams will pass through the materials that have magnetic field-dependent properties [42].

The field distribution of an optical vortex beam in polar coordinates can be expressed mathematically as [43]:

$$E(r, z) = E_0 r^m \exp(im\phi) \exp\left(-\frac{r^2}{\omega(z)^2}\right) \quad \therefore r^2 = x^2 + y^2 \quad (1)$$

where  $E_0$  is the field amplitude,  $\omega(z)$  is the beam width at propagation distance  $z$ , and  $m$  is topological charge. The wavefront, phase profile, and the intensity distribution of vortices have been shown in **Figure 1**.

The vortices can be observed in all the random optical fields, known as speckles, which have random temporal and spatial coherence properties [44, 45]. These patterns can be obtained upon the propagation of coherent random waves through an inhomogeneous media such as ground glass plate (GGP) [46, 47]. This speckle is due to the superposition of many scattered waves originating from the inhomogeneities of the medium [48]. The size of the speckles can be carried by changing the width and wavelength of the beam, and the distribution of speckles can be changed by varying

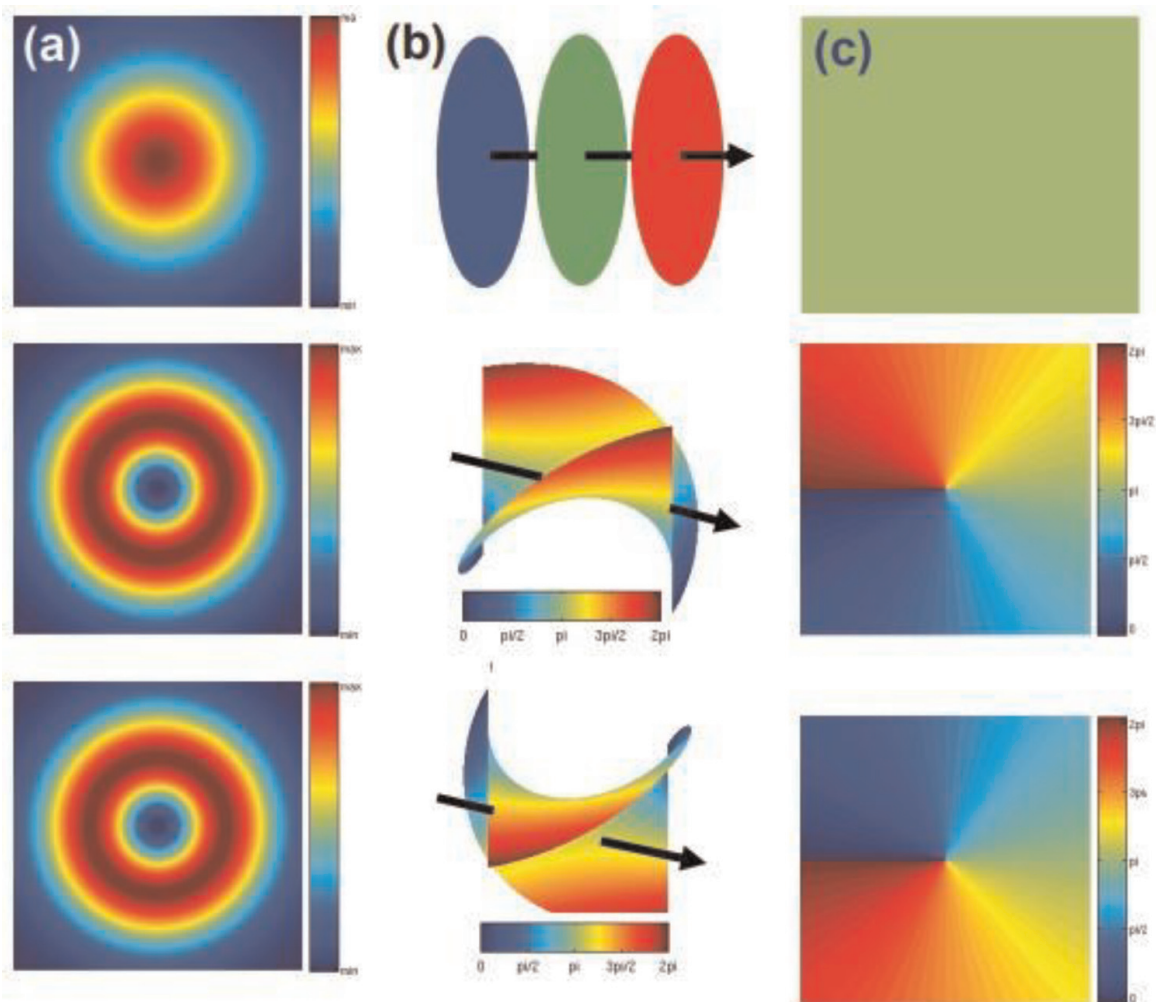


**Figure 1.** The intensity distribution (left), wavefronts (middle), and the phase profiles (right) of optical vortex (OV) beams with  $m = 0$  (top),  $m = +1$  (middle), and  $-1$  (bottom).



**Figure 2.**  
*The speckle patterns generated by the scattering of an optical vortex of order +1 (left), order +2 (middle), and order +3 (right) through the ground glass plate.*

the field distribution incidenting on the rough surface [49–52]. The speckle patterns obtained by the scattering of optical vortices of orders  $m = 1-3$  have been shown in **Figure 2**.

The phase singularities have also been observed in correlation functions and named as coherence vortices [47, 53–55]. The singularities have been verified both theoretically and experimentally using the interferometric techniques. The intensity correlation between the speckle patterns has attained a lot of interest due to their applications in speckle imaging and encryption applications [56–60]. These correlations have been used for finding the roughness of the surface and the effect of turbulence on the spatial modes [61, 62]. The roughness of the surface can be characterized by assuming the delta-correlated random phase screen and well described using a Gaussian correlation function.

In this chapter, we consider the correlations present in the scattered phase singular beams, normal optical vortices, and perfect optical vortices (POVs) for obtaining the information about the spatial mode. We discuss about the coherence vortices which can be obtained through the cross-correlation present in the speckle patterns corresponding to two optical vortices of different orders. We present the intensity distribution and propagation characteristics of coherence vortices by considering the cross-correlations and utilize the autocorrelation measurements for obtaining the mode information. Then we study the correlations present in scattered perfect optical vortices which lead to a new class of coherence functions, Bessel-Gauss functions, and utilized for generating the non-diffracting random fields. We utilized these correlation functions, which are order-dependent although the speckle patterns are order-independent, for encrypting the information which has higher advantage than normal random optical fields.

## **2. Cross-correlations present in scattered optical vortices: realization of coherence vortices**

The phase singularities have been studied extensively in coherent light beams, and in recent days, partially coherent phase singularities have gained a considerable interest due to their robustness against atmospheric propagation [63–65]. The vortices present in partially coherent fields are known as coherence vortices as they can be realized in correlation functions [66–70]. These coherence vortices have been utilized for many applications such as free-space optical communication, remote sensing, and optical imaging [71–75]. The correlation between the two optical random fields plays



an important role in obtaining the various types of coherence functions and their usage in applications, such as optical communication and for producing the physical unclonable functions (PUFs) for cryptography [60, 76–78]. The coherence vortices can be observed in the intensity correlation between two speckle patterns obtained by scattering the coherent vortices of different orders [55, 79]. The coherence vortices can be formulated with mutual coherence function between two speckle patterns corresponding to the vortices of orders  $m_1$  and  $m_2$  and is given by [55, 80]:

$$\tilde{\Gamma}_{m_1, m_2} = A \int r_1^{|m_1|+|m_2|} e^{i(m_1-m_2)\phi_1} e^{-2r_1^2/\omega_0^2} e^{-2i\vec{k}\cdot\vec{r}_1} d\vec{r}_1 \quad (2)$$

One can clearly observe the phase singularity with order  $m = m_1 - m_2$  where  $m$  is the order of the coherence vortex.

For realizing the singularities in coherence functions, we need to scatter the coherent vortex beams through a rough surface such as GGP. The coherent optical vortices can be generated using a computer-generated hologram displayed on a spatial light modulator. After selecting the required vortex beam by an aperture, we scatter these beams through the GGP, and the corresponding speckle patterns are recorded using a CCD camera. We now find the cross-correlation function between two speckle patterns corresponding to optical vortices of different orders using MATLAB software. **Figure 3** shows the speckle patterns along with the determined coherence functions for different values of  $m_1$  and  $m_2$ . It is clear from the figure that the autocorrelation between the speckle patterns provides the coherence function of order

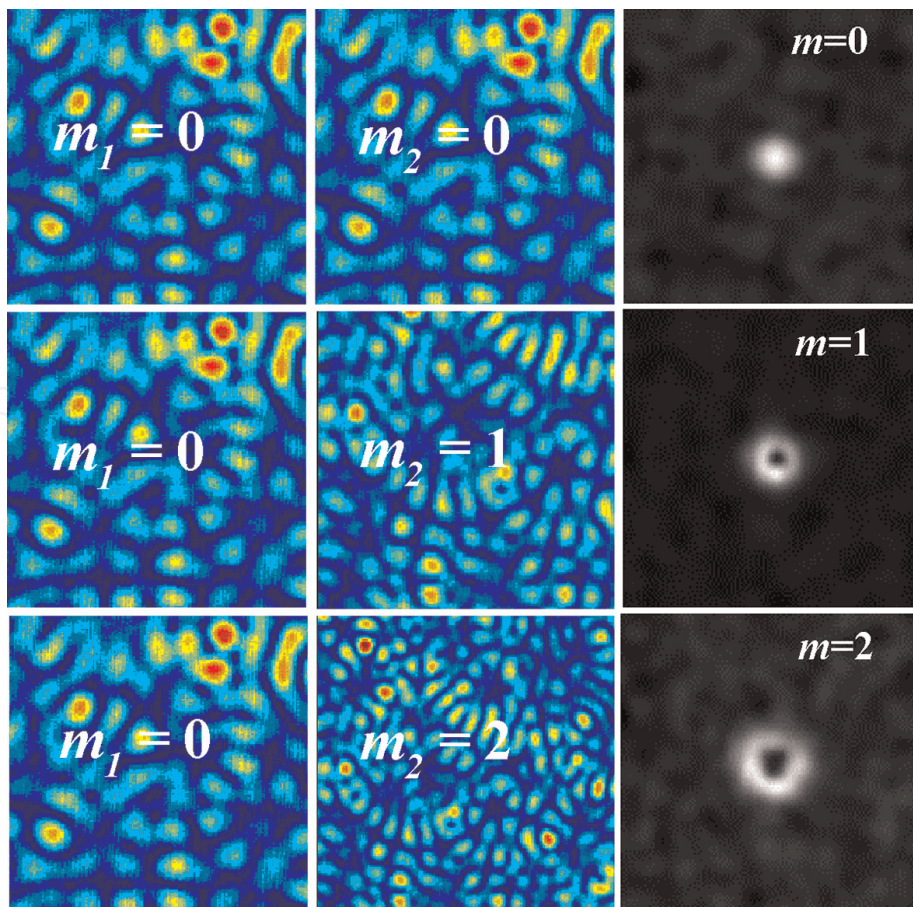


**Figure 3.** The recorded speckle patterns and the corresponding cross-correlation functions, coherence vortices (here  $m = m_2 - m_1$ ).

0. The cross-correlation between the speckle patterns corresponding to two different orders provides the higher-order coherence functions.

The coherence vortices have been characterized through their geometry by considering similarly as that of coherent vortex beams. **Figure 4** shows the intensity distribution of an optical vortex and its line profile along the center for order  $m = 1$ . We characterized the optical vortices by considering them as thin annular rings and using the parameters inner and outer radii  $r_1, r_2$  as shown in figure. These are the nearest (inner) and farthest (outer) radial distances from center at which the intensity falls to  $1/e^2$  (13.6%) of the maximum intensity observed at  $r = r_0$  [46].

**Figure 5** shows the variation of inner and outer radii of the coherence vortex ( $m = m_2 - m_1$ ) of order 2 obtained by considering the cross-correlation between two speckle patterns of different values of  $m_1$  and  $m_2$  (with constant  $m$ ) at the propagation distance of  $z = 20$  cm. We considered the combinations of  $(m_1, m_2) = (0,2), (1,3), (2,4), (3,5), (4,6), (5,7), (6,8)$  where the difference  $(m_2 - m_1)$  is constant.

From the figure, we observe that the inner and outer radii for all the combinations mentioned earlier are constant and independent of the input vortex beams considered for scattering. From this, we confirm that the intensity distribution of coherence

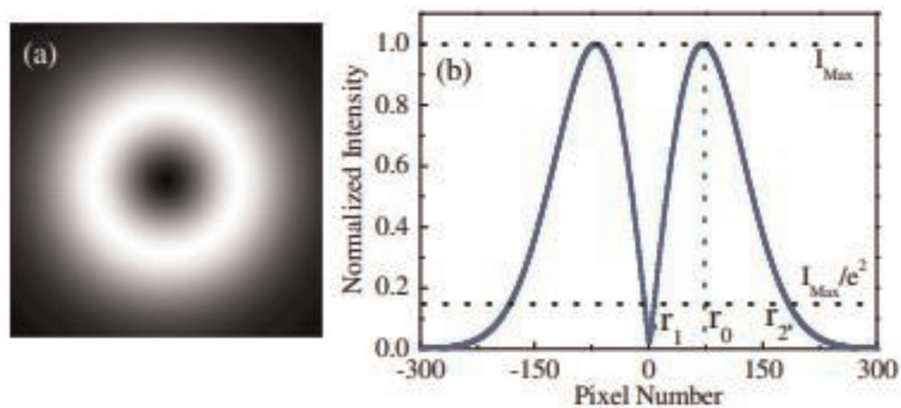


**Figure 4.**  
 (a) Intensity distribution and (b) line profile through its center for an optical vortex of order 1.

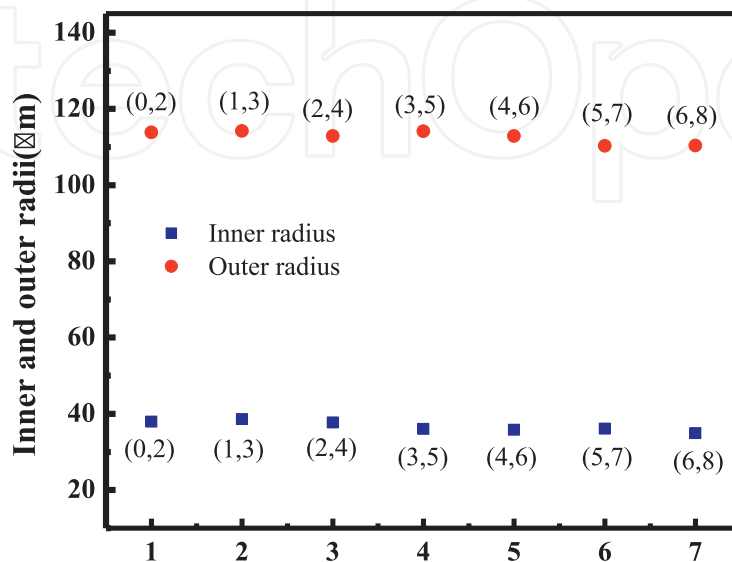


**Figure 5.**  
 Variation of inner and outer radii of the coherence vortex of order 2 with different combinations of input vortex beams.

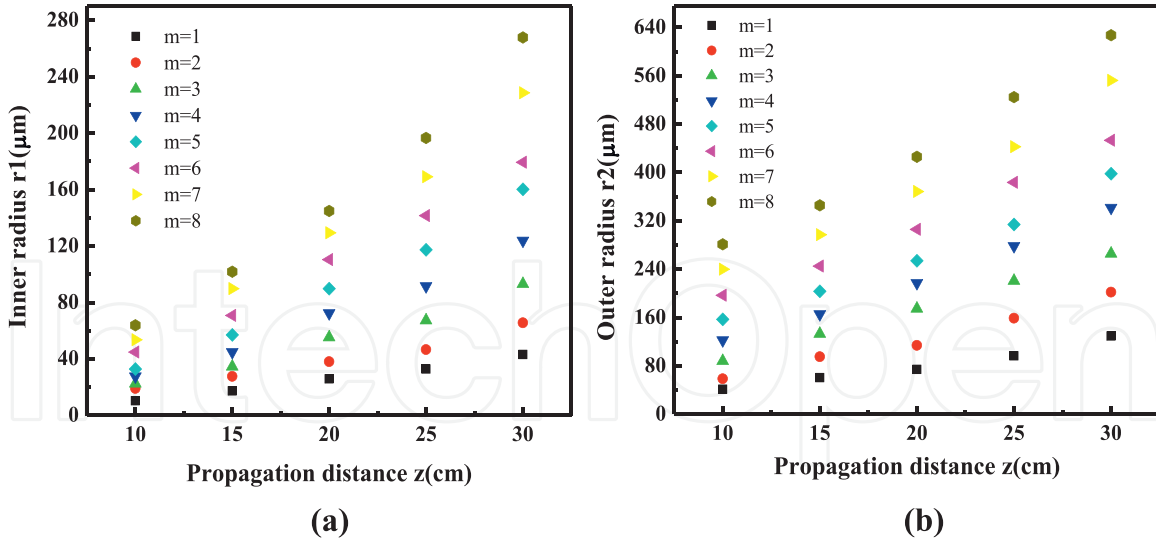


**Figure 6.** Variation of inner (a) and outer (b) radii for coherence vortices of order  $m = 1-8$  with the propagation distance  $z$ .

vortices depends only on the order difference but not on the individual orders of the optical vortices considered for scattering.

Now, we study the propagation characteristics of these coherence vortices.

**Figure 6a** and **6b** show the variation of inner and outer radii for different orders  $m = 1-8$  with respect to the propagation distance from  $z = 10-30$  cm. The speckles have been recorded from  $z = 10-30$  cm at an interval of 5 cm. It is observed that the inner and outer radii from figure vary linearly with the propagation distance for all orders and increase with order as shown in **Figure 6**.

We consider the rate of change of inner and outer radii with propagation distance as divergence and can be obtained by finding the slope of the line drawn between inner or outer radius and the propagation distance [79, 81, 82]. The slope has been determined using the linear fit to the experimental data. The variation of divergence with the order by considering inner and outer radii has been shown in **Figure 7**. It is clear from the figure that the divergence increases linearly with order ( $m$ ). One can utilize the inner and outer radii at the source plane and their divergence for

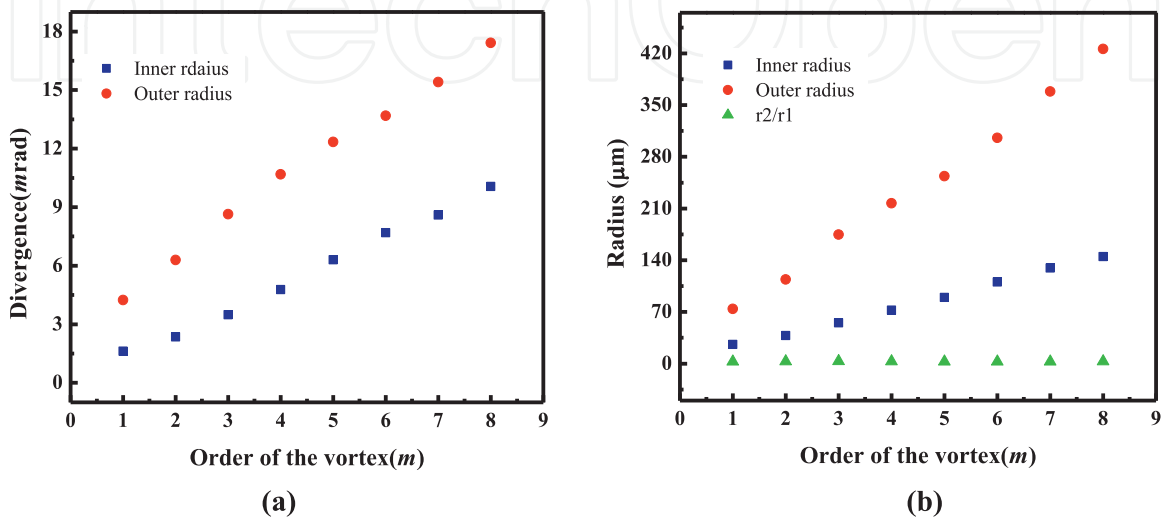


**Figure 7.** Variation of inner and outer radii along with their divergence as a function of order of the coherence functions.

characterizing the order of a coherence vortex. One can also find the information about the incident spatial modes using these coherence vortices.

### 3. Autocorrelation studies for scattered optical vortices

For the applications in free-space optical communication using spatial modes, one needs to propagate these modes for longer distances. After propagating through the channel, the mode information gets disturbed, and one needs to find the mode information of these perturbed beams. Although there are many techniques to find the order of a higher-order coherent optical vortex [46], they are not suitable for partially coherent or incoherent vortices. A limited number of techniques are available for finding the order of a partially coherent vortex beam. In this section, we study the autocorrelation properties of scattered optical vortices for diagnosing the spatial mode information [83–85]. The number of zero points or dark rings present in 2D spatial correlation function provides the information about the spatial mode. The spatial autocorrelation function of a perturbed optical vortex is equivalent to the Fourier transform (FT) of its intensity in the source plane [86]. The number of dark rings presented in the spatial correlation function is equal to the topological charge of vortex beam which has also been verified by verifying the number of zero points present in Fourier transform of a coherent vortex beam which further will be discussed. Here, we show that the existence of the ring dislocations in the spatial correlation function corresponds to the scattering of the optical vortex field [87].

The theoretical background for the 2D autocorrelation function starts by assuming the field distribution of Laguerre-Gaussian beam with azimuthal index  $m$  and zero radial index in the source plane ( $z = 0$ ) in cylindrical coordinates as:

$$E(\rho, \theta, 0) \propto \rho^{|m|} \exp\left(\frac{-\rho^2}{\omega_0^2}\right) \exp(im\theta) \quad (3)$$

where  $\omega_0$  is beam waist of the input beam and  $(\rho, \theta)$  are the cylindrical coordinates in incident plane. The scattering of optical vortex (OV) beams through a ground glass plate (GGP) that can be well described by a random phase function  $\exp(i\Phi)$  where  $\Phi$  varies randomly from 0 to  $2\pi$ . A particular way of obtaining this type of phase distribution  $\Phi$  is by taking a 2D convolution between a random spatial function and a Gaussian correlation function [44]. The field  $U(\rho, \theta)$  after the GGP can be obtained from the incident field  $E(\rho, \theta)$  and can be written as:

$$U(\rho, \theta) \propto \exp(i\Phi)E(\rho, \theta) \quad (4)$$

where the autocorrelation of the phase exponential factor is a Dirac-delta function at plane  $(\rho, \theta)$ , which can be written mathematically as:

$$\langle \exp[i(\Phi(\rho_1, \theta_1) - \Phi(\rho_2, \theta_2))] \rangle = \delta(\rho_1 - \rho_2)\delta(\theta_1 - \theta_2) \quad (5)$$

where  $\langle a \rangle$  denotes the ensemble average operation in  $a$ . The autocorrelation function between two speckle patterns of same order obtained by scattering of OV beams through GGP is given by:

$$\Gamma(r_1, \varphi_1; r_2, \varphi_2) = \langle U_1(r_1, \varphi_1)U_2^*(r_2, \varphi_2) \rangle \quad (6)$$



where  $(r, \varphi)$  are the coordinates at the detection plane. The field at the detection plane in terms of field at the incident plane can be evaluated using Fresnel's diffraction integral in cylindrical coordinates as [88, 89]:

$$U(r, \varphi, z) = \frac{e^{ikz}}{i\lambda z} \int \rho d\rho \int d\theta U(\rho, \theta) e^{\left\{ \frac{ik}{2z}(\rho^2 + r^2 - 2\rho r \cos(\theta - \varphi)) \right\}} \quad (7)$$

Using Eq. (7) and Eq. (6), we have that

$$\begin{aligned} \Gamma(r_1, \varphi_1; r_2, \varphi_2) &= \langle U_1(r_1, \varphi_1) U_2^*(r_2, \varphi_2) \rangle \\ &= \left\langle \frac{e^{ikz}}{i\lambda z} \int \rho_1 d\rho_1 \int d\theta_1 U_1(\rho_1, \theta_1) e^{\left\{ \frac{ik}{2z}(\rho_1^2 + r_1^2 - 2\rho_1 r_1 \cos(\theta_1 - \varphi_1)) \right\}} \right. \\ &\quad \times \left. \frac{e^{-ikz}}{-i\lambda z} \int \rho_2 d\rho_2 \int d\theta_2 U_2^*(\rho_2, \theta_2) e^{\left\{ \frac{-ik}{2z}(\rho_2^2 + r_2^2 - 2\rho_2 r_2 \cos(\theta_2 - \varphi_2)) \right\}} \right\rangle \\ &= \frac{e^{\left\{ \frac{ik}{2z}[r_1^2 - r_2^2] \right\}}}{\lambda^2 z^2} \int \rho_1 d\rho_1 \int d\theta_1 \int \rho_2 d\rho_2 \int d\theta_2 \langle U_1(\rho_1, \theta_1) U_2^*(\rho_2, \theta_2) \rangle \\ &\quad \times e^{\left\{ \frac{ik}{2z}(\rho_1^2 - \rho_2^2 - 2\rho_1 r_1 \cos(\theta_1 - \varphi_1) + 2\rho_2 r_2 \cos(\theta_2 - \varphi_2)) \right\}} \end{aligned} \quad (8)$$

which is a fourfold integral and includes cross-correlation of field at the incident plane  $(\rho, \theta)$  namely,  $\langle U_1(\rho_1, \theta_1) U_2^*(\rho_2, \theta_2) \rangle$ . Using Eq. (4) and Eq. (5), we get the cross-correlation function as

$$\begin{aligned} \langle U_1(\rho_1, \theta_1) U_2^*(\rho_2, \theta_2) \rangle &= \langle E_1(\rho_1, \theta_1) e^{i\Phi(\rho_1, \theta_1)} E_2^*(\rho_2, \theta_2) e^{i\Phi(\rho_2, \theta_2)} \rangle \\ &= E_1(\rho_1, \theta_1) E_2^*(\rho_2, \theta_2) \langle e^{i(\Phi(\rho_1, \theta_1) - \Phi(\rho_2, \theta_2))} \rangle \\ &= E_1(\rho_1, \theta_1) E_2^*(\rho_2, \theta_2) \times \delta(\rho_1 - \rho_2) \delta(\theta_1 - \theta_2) \end{aligned} \quad (9)$$

The ground glass plate (random phase screen) is modeled as a  $\delta$ -correlated phase function. The autocorrelation function after using the same is

$$\langle U_1(\rho_1, \theta_1) U_2^*(\rho_2, \theta_2) \rangle = E(\rho_1, \theta_1) E^*(\rho_2, \theta_2) \quad (10)$$

Using Eq. (10) in Eq. (9) and the properties of the Dirac-delta function, the fourfold integral of the autocorrelation is reduced to the two-fold integral as:

$$\begin{aligned} \Gamma(r_1, \varphi_1; r_2, \varphi_2) &= \langle U_1(r_1, \varphi_1) U_2^*(r_2, \varphi_2) \rangle \\ &= \frac{e^{\left\{ \frac{ik}{2z}[r_1^2 - r_2^2] \right\}}}{\lambda^2 z^2} \int \rho d\rho \int d\theta E(\rho, \theta) E^*(\rho, \theta) \end{aligned} \quad (11)$$

$$\begin{aligned} \Gamma_{12}(\Delta r) &= \frac{e^{\left\{ \frac{ik}{2z}[r_1^2 - r_2^2] \right\}}}{\lambda^2 z^2} \iint |E(\rho, \theta)|^2 \exp \left[ -\frac{ik}{z}(\rho \Delta r \cos(\varphi_s - \theta)) \right] \rho d\rho d\theta \end{aligned} \quad (12)$$

where  $\Delta r \cos(\varphi_s - \theta) = [(r_1 \cos(\varphi_1) - r_2 \cos(\varphi_2)) \cos \theta] + [(r_1 \sin(\varphi_1) - r_2 \sin(\varphi_2)) \sin \theta]$  and  $\Delta r^2 = r_1^2 + r_2^2 - 2r_1r_2 \cos(\varphi_2 - \varphi_1)$ .

Using Eq. (3), the absolute value of the field distribution is

$$|E(\rho, \phi, 0)|^2 = \rho^{2|m|} \exp\left(\frac{-2\rho^2}{\omega_0^2}\right) \quad (13)$$

Let us calculate the integral part of the correlation as

$$\begin{aligned} \Gamma_{12}(\Delta r) &= \frac{e^{\left\{\frac{ik}{2z}[r_1^2 - r_2^2]\right\}}}{\lambda^2 z^2} \iint \rho^{2|m|} \exp\left(\frac{-2\rho^2}{\omega_0^2}\right) \exp\left[-\frac{ik}{z}(\rho \Delta r \cos(\varphi_s - \theta))\right] \rho d\rho d\theta \\ &= \int \rho^{2|m|+1} \exp\left(\frac{-2\rho^2}{\omega_0^2}\right) d\rho \int \exp\left[-\frac{ik}{z}(\rho \Delta r \cos(\varphi_s - \theta))\right] d\theta \end{aligned} \quad (14)$$

and  $I' = \int \exp\left[-\frac{ik}{z}(\rho \Delta r \cos(\varphi_s - \theta))\right] d\theta$  can be calculated by using Anger-Jacobi identity  $e^{-iz \cos \theta} = \sum_{n=-\infty}^{\infty} (-1)^n i^n J_n(z) e^{in\theta}$ , we get [90]

$$I' = \int \exp\left[-\frac{ik}{z}(\rho \Delta r \cos(\varphi_s - \theta))\right] d\theta = 2\pi J_0\left(\frac{k\rho}{z} \Delta r\right) \quad (15)$$

Substitute the aforementioned equation in Eq. (14), then the far-field autocorrelation function or the Fourier transform of the incident intensity in the source plane becomes

$$\Gamma_{12}(\Delta r) = \frac{2\pi e^{\left\{\frac{ik}{2z}[r_1^2 - r_2^2]\right\}}}{\lambda^2 z^2} \int_0^{\infty} \rho^{2|m|+1} \exp\left(\frac{-2\rho^2}{\omega_0^2}\right) J_0\left(\frac{k\rho}{z} \Delta r\right) d\rho \quad (16)$$

where  $J_0\left(\frac{k\rho}{z} \Delta r\right)$  represents the zeroth-order Bessel function. Using the following integral,

$$\int_0^{\infty} x^\mu \exp(-\alpha x^2) J_\nu(xy) dx = \frac{y^\nu \Gamma\left(\frac{1}{2}(\mu - \nu + 1)\right)}{2^{\nu+1} \alpha^{\frac{1}{2}(\mu + \nu + 1)}} \exp\left(\frac{-y^2}{4\alpha}\right) L_{\frac{1}{2}(\mu - \nu + 1)}^\nu\left(\frac{y^2}{4\alpha}\right) \quad (17)$$

From Eqs. (16) and (17), the mutual coherence function will become

$$\Gamma_{12}(\Delta r) = \frac{\pi \omega_0^{2|m|+2} e^{\left\{\frac{ik}{2z}[r_1^2 - r_2^2]\right\}}}{2^{|m|+1} \lambda^2 z^2} \exp\left(\frac{-k^2 \omega_0^2 \Delta r^2}{8z^2}\right) L_{|m|}\left(\frac{k^2 \omega_0^2 \Delta r^2}{8z^2}\right) \quad (18)$$

where  $\mu = 2|m| + 1, \alpha = \frac{2}{\omega_0^2}, y = \frac{k}{z} \Delta r, \nu = 0$  and  $L_{|m|}\left(\frac{k^2 \omega_0^2 \Delta r^2}{8z^2}\right)$  represents the Laguerre polynomial of order  $m$ . The aforementioned equation represents the autocorrelation of scattered Laguerre-Gaussian (LG) beam, and it depends on the azimuthal index and propagation distance. In the spatial correlation field, the number of dark rings or number of zero points in the Laguerre polynomial gives the information about the order or azimuthal index of the vortex beam. We verify these theoretical findings experimentally, and the details are given as follows.

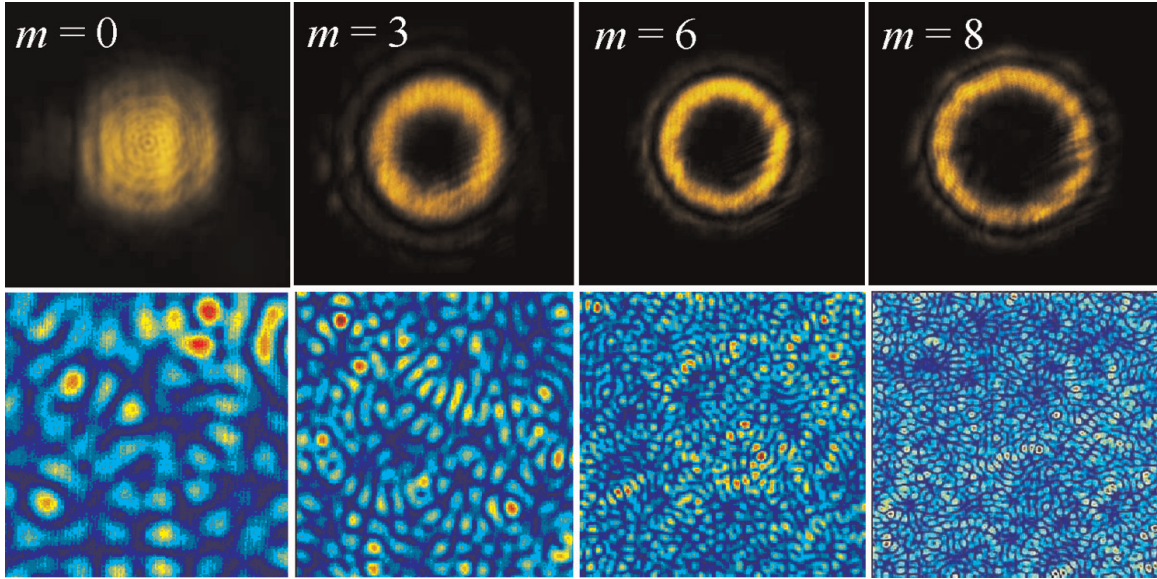


**Figure 8.**  
Intensity distributions of optical vortices and their corresponding speckle patterns.

We have generated the optical vortices of orders  $m = 0-8$  by displaying a computer-generated hologram on a spatial light modulator and scatter them through a GGP. We have shown the intensity distributions of optical vortices at the plane of GGP and the corresponding speckle patterns in **Figure 8** which have been recorded using a CCD camera. It is clear from the figure that the size of the speckles decreases with the increase in order, and we observe the structures in speckle distributions corresponding to higher orders.

Further, we have processed the speckle patterns for finding the autocorrelation function using MATLAB software. We found that the order or topological charge of a given spatial mode is given by the number of dark rings present in the autocorrelation function. This method is suitable for vortices with low topological charges. However, as we increase the order, we must identify the number of dark rings carefully because the adjacent two dark rings are very close to each other, and it is very difficult to distinguish them. This technique is alignment free as the autocorrelation function does not depend on the alignment. **Figure 9** shows the experimentally obtained spatial autocorrelation functions (top) for the speckle patterns corresponding to the vortices of orders  $m = 0-3$  from left and right. The results are in good agreement with the theoretically obtained correlation function as shown in bottom row of the figure. It is clear from the figure that the order of vortex is equal to the number of dark rings present in the spatial autocorrelation field. One can also utilize the propagation characteristics for the better diagnosis of the information of a given spatial mode.

The generalized theory for autocorrelation functions of LG beams with nonzero radial index is provided and experimentally verified as well. The number of dark rings is equal to the sum of twice the radial index and azimuthal index [86]. The autocorrelation function of a scattered LG beam with nonzero radial and azimuthal indices is given by [91]:

$$\chi(\xi) = \frac{\pi\omega_0^{2|m|+2}}{2^{|m|+1}} \frac{(p+|m|)!}{p!} \exp\left(-\frac{\pi^2\omega_0^2\xi^2}{2}\right) L_p\left(-\frac{\pi^2\omega_0^2\xi^2}{2}\right) L_{p+|m|}\left(-\frac{\pi^2\omega_0^2\xi^2}{2}\right) \quad (19)$$

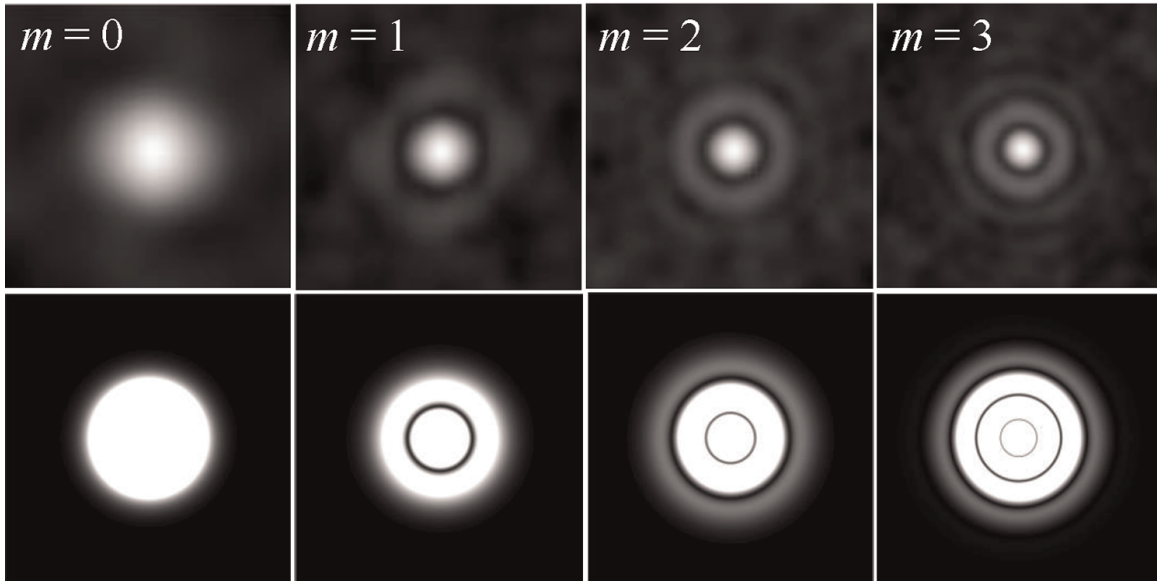


**Figure 9.** Experimental (top) and theoretical (bottom) 2D spatial autocorrelation function for a speckle pattern generated by scattering a vortex beams of orders  $m = 0-3$  from left to right.

where  $p$  is the radial index and  $m$  is the azimuthal index of a LG beam. We need to study the following subcases from the aforementioned expression for the better understanding of correlation function:

- i. If  $p = 0$ , then the correlation function corresponds to the optical vortices that carry OAM and is given by:

$$\chi(\xi) = \frac{\pi\omega_0^{2|m|+2}}{2^{|m|+1}} |m|! \exp\left(-\frac{\pi^2\omega_0^2\xi^2}{2}\right) L_{|m|}\left(-\frac{\pi^2\omega_0^2\xi^2}{2}\right) \quad (20)$$

The aforementioned expression is exactly matching with our equation obtained for LG beams with zero radial index.

- ii. If  $m = 0$  (non-vortex beams), then the autocorrelation function is given by:

$$\chi(\xi) = \frac{\pi\omega_0^2}{2} \exp\left(-\frac{\pi^2\omega_0^2\xi^2}{2}\right) \left(L_p\left(-\frac{\pi^2\omega_0^2\xi^2}{2}\right)\right)^2 \quad (21)$$

From Eqs. (19), (20), and (21), one can obtain the relation between number of dark rings and radial and azimuthal indices as:

$$\begin{aligned} N &= 2p + |m| \quad \text{when } m \neq 0 \\ &= p \quad \text{when } m = 0. \end{aligned} \quad (22)$$

where  $N$  is the number of dark rings present in the autocorrelation function.

The numerical results for the LG beams of nonzero radial index have been shown in **Figure 10**. We can observe the number of dark rings in the far-field autocorrelation function which depends on both radial and azimuthal indices. The radial and azimuthal indices for the contour plots are (a)  $m = 1, p = 1$ ; (b)  $m = 2, p = 1$ ; (c)  $m = 3, p = 1$ ; (d)  $m = 1, p = 2$ ; (e)  $m = 2, p = 2$ ; and (f)  $m = 3, p = 2$ .



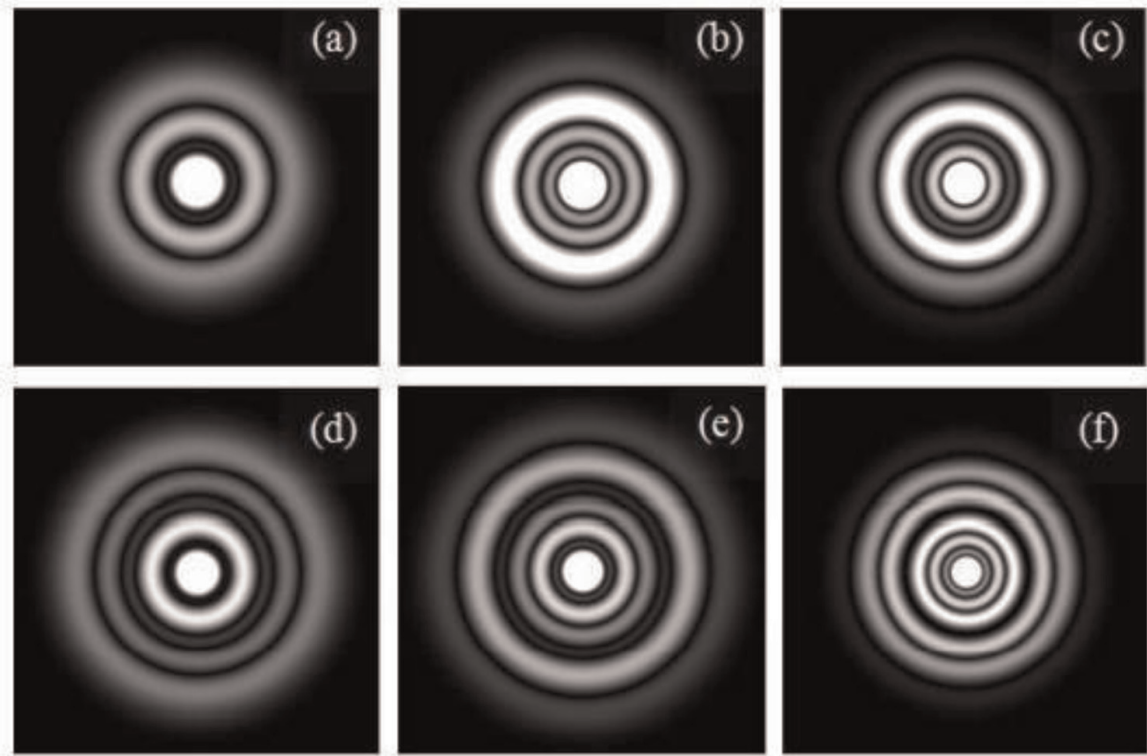


**Figure 10.**  
*Theoretical far-field auto-correlation function with different combinations of radial and azimuthal indices: (a)  $m = 1, p = 1$ ; (b)  $m = 2, p = 1$ ; (c)  $m = 3, p = 1$ ; (d)  $m = 1, p = 2$ ; (e)  $m = 2, p = 2$ ; (f)  $m = 3, p = 2$ .*

Now, we verify Van Cittert-Zernike theorem states that the autocorrelation function of a scattered light beam is same as the Fourier transform (FT) of intensity distribution incident on the rough surface, i.e. source plane. Here, we present the results obtained for the FT of intensity distribution of a LG beam in which the number of dark rings is equal to the order of the vortex [92] as shown in **Figure 11**.

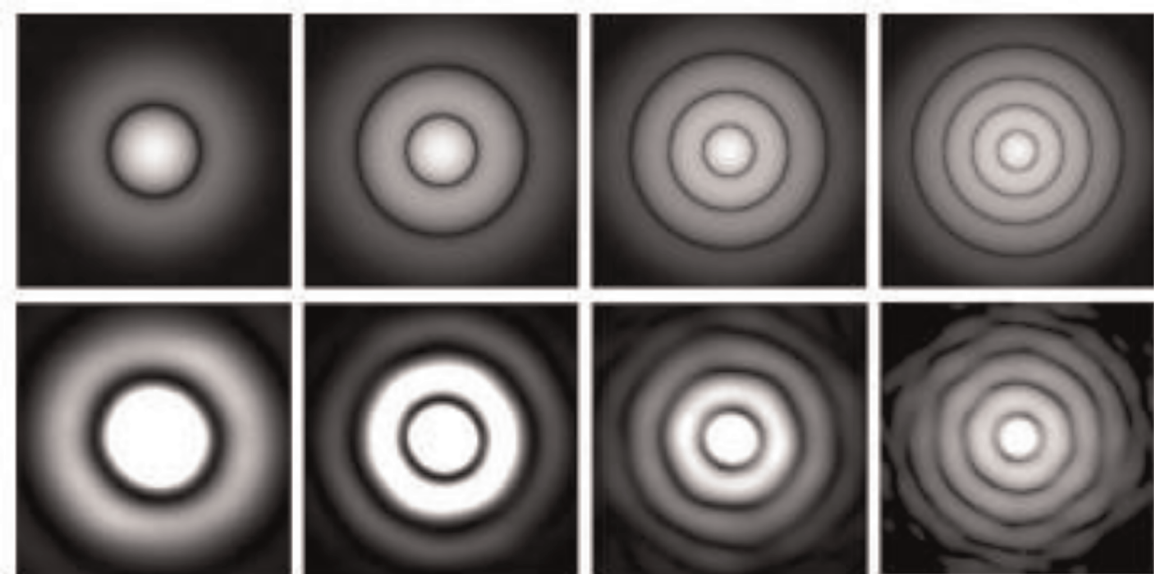


**Figure 11.**  
*The theoretical and experimental Fourier transform contour plots for the intensity distribution of LG beams with azimuthal index  $m = 1-4$  from left to right.*

### 3.1 Correlations in scattered perfect optical vortices

From the aforementioned discussions, it is known that the field and intensity distributions of an optical vortex are strongly influenced by its topological charge which may be a drawback for controlling them while they propagate through optical channels [93]. To overcome this, another class of vortices has been introduced, known as perfect optical vortices (POVs) with order-independent intensity distribution [94]. The POV beams are known for very thin annular rings whose width and radius are independent of topological charge [95–98]. The POV beams can be generated experimentally by Fourier transforming Bessel-Gauss beams which will be generated by passing optical vortex beams through an axicon [99–101]. The radius and width of the ring of a POV beam can easily be controlled by changing the apex angle or axicon parameter [100, 102]. We study the correlations present in scattered POV beams and utilize for generating the non-diffracting optical random fields [103]. The theoretical analysis for the cross-correlation between two speckle patterns obtained by scattering POV beams of different orders is as follows:

The field distribution of a perfect optical vortex (POV) beam, described by a thin annular ring of order  $m$ , which can be represented mathematically as:

$$E(\rho, \theta) = \delta(\rho - \rho_0)e^{im\theta} \quad (23)$$

where  $\rho_0$  is the radius of the POV beam and  $\delta$  represents the Dirac-delta function. In practical, the POV beams can be realized with finite ring width which can be represented mathematically as:

$$E(\rho, \theta) = g(\rho - \rho_0; \varepsilon)e^{im\theta} \quad (24)$$

where  $g(\rho - \rho_0; \varepsilon)$  is a narrow function in the radial direction with a finite “width”  $\varepsilon$ , such as Gaussian and height proportional to  $1/\varepsilon$ . The scattered field  $U(\rho, \theta)$  after the GGP can be obtained from the incident field  $E(\rho, \theta)$  on the GGP as

$$U(\rho, \theta) = e^{i\Phi(\rho, \theta)}E(\rho, \theta) \quad (25)$$

where the cross-correlation of the phase exponential factor is a Dirac-delta function at plane  $(\rho, \theta)$ , which implies the mutually independent inhomogeneities that can be expressed mathematically as:

$$\langle e^{i[\Phi(\rho_1, \theta_1) - \Phi(\rho_2, \theta_2)]} \rangle = \delta(\rho_1 - \rho_2)\delta(\theta_1 - \theta_2) \quad (26)$$

where  $\langle a \rangle$  denotes the ensemble average operation in  $a$  [9]. The mutual coherence function between the two scattered POV fields at a distance of  $z$  from the GGP is given by:

$$\Gamma(r_1, \varphi_1; r_2, \varphi_2) = \langle U_1(r_1, \varphi_1)U_2^*(r_2, \varphi_2) \rangle \quad (27)$$

where  $\rho$  and  $\theta$  are source plane coordinates, and  $r$  and  $\varphi$  are detection plane coordinates. The field at detection plane can be obtained using Fresnel diffraction integral in cylindrical coordinates as: [88, 89]

$$U(r, \varphi, z) = \frac{e^{ikz}}{i\lambda z} \int \rho d\rho \int d\theta U(\rho, \theta) e^{\left\{ \frac{ik}{2z}(\rho^2 + r^2 - 2\rho r \cos(\theta - \varphi)) \right\}} \quad (28)$$

From Eq. (27) and Eq. (28), we have

$$\begin{aligned}
 \Gamma(r_1, \varphi_1; r_2, \varphi_2) &= \langle U_1(r_1, \varphi_1) U_2^*(r_2, \varphi_2) \rangle \\
 &= \left\langle \frac{e^{ikz}}{i\lambda z} \int \rho_1 d\rho_1 \int d\theta_1 U_1(\rho_1, \theta_1) e^{\left\{ \frac{ik}{2z} (\rho_1^2 + r_1^2 - 2\rho_1 r_1 \cos(\theta_1 - \varphi_1)) \right\}} \right. \\
 &\quad \times \left. \frac{e^{-ikz}}{-i\lambda z} \int \rho_2 d\rho_2 \int d\theta_2 U_2^*(\rho_2, \theta_2) e^{\left\{ \frac{-ik}{2z} (\rho_2^2 + r_2^2 - 2\rho_2 r_2 \cos(\theta_2 - \varphi_2)) \right\}} \right\rangle \quad (29) \\
 &= \frac{e^{\left\{ \frac{ik}{2z} [r_1^2 - r_2^2] \right\}}}{\lambda^2 z^2} \int \rho_1 d\rho_1 \int d\theta_1 \int \rho_2 d\rho_2 \int d\theta_2 \langle U_1(\rho_1, \theta_1) U_2^*(\rho_2, \theta_2) \rangle \\
 &\quad \times e^{\left\{ \frac{ik}{2z} (\rho_1^2 - \rho_2^2 - 2\rho_1 r_1 \cos(\theta_1 - \varphi_1) + 2\rho_2 r_2 \cos(\theta_2 - \varphi_2)) \right\}}
 \end{aligned}$$

which is a fourfold integral, and this integral includes the cross-correlation of the field at the incident plane  $(\rho, \theta)$ , namely,  $\langle U_1(\rho_1, \theta_1) U_2^*(\rho_2, \theta_2) \rangle$ . Using Eqs. (24) and (25), we can get the cross-correlation function at plane  $(\rho, \theta)$  as:

$$\begin{aligned}
 \langle U_1(\rho_1, \theta_1) U_2^*(\rho_2, \theta_2) \rangle &= \langle E_1(\rho_1, \theta_1) e^{i\Phi(\rho_1, \theta_1)} E_2^*(\rho_2, \theta_2) e^{i\Phi(\rho_2, \theta_2)} \rangle \\
 &= E_1(\rho_1, \theta_1) E_2^*(\rho_2, \theta_2) \langle e^{i(\Phi(\rho_1, \theta_1) - \Phi(\rho_2, \theta_2))} \rangle \quad (30) \\
 &= E_1(\rho_1, \theta_1) E_2^*(\rho_2, \theta_2) \times \delta(\rho_1 - \rho_2) \delta(\theta_1 - \theta_2)
 \end{aligned}$$

Using Eq. (30) in Eq. (29) and the properties of the Dirac-delta function, the fourfold integral of the cross-correlation is reduced to the twofold integral as:

$$\begin{aligned}
 \Gamma(r_1, \varphi_1; r_2, \varphi_2) &= \langle U_1(r_1, \varphi_1) U_2^*(r_2, \varphi_2) \rangle \\
 &= \frac{e^{\left\{ \frac{ik}{2z} [r_1^2 - r_2^2] \right\}}}{\lambda^2 z^2} \int \rho_1 d\rho_1 \int d\theta_1 E_1(\rho_1, \theta_1) E_2^*(\rho_1, \theta_1) \quad (31) \\
 &\quad \times e^{\left\{ \frac{-ik}{z} (\rho_1 \cos(\theta_1 - \varphi_1) - r_2 \cos(\theta_1 - \varphi_2)) \right\}}
 \end{aligned}$$

In the special case of incident POV beams, we can use Eq. (24) to write

$$E_1(\rho_1, \theta_1) E_2^*(\rho_1, \theta_1) = g(\rho_1 - \rho_{01}; \varepsilon) g(\rho_1 - \rho_{02}; \varepsilon) e^{i(m_1 \theta_1 - m_2 \theta_1)} \quad (32)$$

As we know that the radius of POV beams is independent of order, i.e.  $\rho_{01} = \rho_{02} = \rho_0$ , therefore

$$E_1(\rho_1, \theta_1) E_2^*(\rho_1, \theta_1) = g^2(\rho_1 - \rho_0; \varepsilon) e^{i(m_1 - m_2) \theta_1} \quad (33)$$

Under the condition  $\varepsilon \rightarrow 0$ , one can replace  $g^2(\rho - \rho_0; \varepsilon)$  with a single Dirac-delta function  $\delta(\rho - \rho_0)$  and the aforementioned expression becomes

$$E_1(\rho_1, \theta_1) E_2^*(\rho_1, \theta_1) = \delta(\rho_1 - \rho_0) e^{i(m_1 - m_2) \theta_1} \quad (34)$$

After substituting Eq. (34) in Eq. (31), we get

$$\Gamma(r_1, \varphi_1; r_2, \varphi_2) = \frac{e^{\left\{\frac{ik}{2z}[r_1^2 - r_2^2]\right\}}}{\lambda^2 z^2} \int \rho_1 d\rho_1 \int d\theta_1 \delta(\rho_1 - \rho_0) e^{i(m_1 - m_2)\theta_1} e^{\left\{\frac{-ik}{z}\rho(r_1 \cos(\theta_1 - \varphi_1) - r_2 \cos(\theta_1 - \varphi_2))\right\}} \quad (35)$$

The integral in the aforementioned equation can be evaluated as:

$$\begin{aligned} I &= \int \delta(\rho_1 - \rho_0) \rho_1 d\rho_1 \int e^{i(m_1 - m_2)\theta_1} e^{\frac{-ik}{z}\rho(r_1 \cos(\theta_1 - \varphi_1) - r_2 \cos(\theta_1 - \varphi_2))} d\theta_1 \\ &= \int \delta(\rho_1 - \rho_0) \rho_1 d\rho_1 \int e^{i(m_1 - m_2)\theta_1} e^{\frac{-ik}{z}(\rho \Delta r \cos(\varphi_s - \theta_1))} d\theta_1 \end{aligned} \quad (36)$$

For solving the integral of  $\theta_1$ , we assume that  $\theta' = \varphi_s - \theta_1$  then we get the integral as:

$$I = e^{i(m_1 - m_2)\varphi_s} \int \delta(\rho_1 - \rho_0) \rho_1 d\rho_1 \int e^{i(m_1 - m_2)\theta'} e^{\frac{-ik}{z}(\rho \Delta r \cos \theta')} d\theta' \quad (37)$$

where  $\theta'$  varies from  $-\varphi_s$  to  $2\pi - \varphi_s$  and using Anger-Jacobi identity  $e^{-iz \cos \theta} = \sum_{n=-\infty}^{\infty} (-1)^n i^n J_n(z) e^{in\theta}$ , we get [90]

$$I = e^{i(m_1 - m_2)\varphi_s} \int \delta(\rho_1 - \rho_0) \rho_1 d\rho_1 \sum_{n=-\infty}^{\infty} (-1)^n i^n J_n\left(\frac{k\rho}{z} \Delta r\right) \int e^{in\theta'} e^{i(m_1 - m_2)\theta'} d\theta' \quad (38)$$

The aforementioned integral has nonzero value only when  $n = m_2 - m_1$  and the integral becomes

$$I = 2\pi e^{i(m_1 - m_2)\varphi_s} \int \delta(\rho_1 - \rho_0) \rho_1 d\rho_1 (-1)^{m_2 - m_1} i^{m_2 - m_1} J_{m_2 - m_1}\left(\frac{k\rho}{z} \Delta r\right) \quad (39)$$

By using the integral properties of Dirac-delta function [90], we get that

$$I = 2\pi \rho_0 (-i)^{m_2 - m_1} e^{i(m_1 - m_2)\varphi_s} J_{m_2 - m_1}\left(\frac{k\rho_0}{z} \Delta r\right) \quad (40)$$

Now, the cross-correlation function as defined in Eq. (35) becomes

$$\Gamma_{12}(\Delta r) = \frac{2\pi \rho_0 (-i)^{m_2 - m_1} e^{\frac{ik}{2z}(r_1^2 - r_2^2)}}{\lambda^2 z^2} e^{i(m_1 - m_2)\varphi_s} J_{m_2 - m_1}\left(\frac{k\rho_0}{z} \Delta r\right) \quad (41)$$

The aforementioned equation representing the mutual coherence function of two speckle patterns is described well by the Bessel function of order  $m = m_2 - m_1$ . The corresponding cross-correlation function of two speckle patterns is given by:

$$C(\Delta r) = (-i)^{m_2 - m_1} e^{i(m_1 - m_2)\varphi_s} J_{m_2 - m_1}\left(\frac{k\rho_0}{z} \Delta r\right) \quad (42)$$

Normalized intensity distribution of the coherence function can be evaluated in terms of time-averaged intensity  $I_0$  as:

$$I(\Delta r) = I_0^2 \left(1 + |C(\Delta r)|^2\right) = I_0^2 \left(1 + J_{m_2 - m_1}^2\left(\frac{k\rho_0}{z} \Delta r\right)\right) \quad (43)$$



If two speckle patterns correspond to the same order, the cross-correlation function is converted into an autocorrelation function, which can be obtained by keeping  $m_1 = m_2$  in the aforementioned equation. We obtain the autocorrelation function as:

$$I(\Delta r) = I_0^2 \left( 1 + J_0^2 \left( \frac{k\rho_0}{z} \Delta r \right) \right) \quad (44)$$

It is clear from the aforementioned analysis that the autocorrelation functions can be described with Bessel functions of order zero and cross-correlation functions can be described with Bessel functions of nonzero orders ( $m = m_2 - m_1$ ).

The experimental validation of aforementioned theoretical findings has been done and the details are as follows: **Figure 12** shows the speckle patterns generated by the scattering of POV beams and the corresponding cross-correlation functions. From the figure, we confirm the Bessel-Gauss nature of coherence functions with order  $m = m_2 - m_1$ .

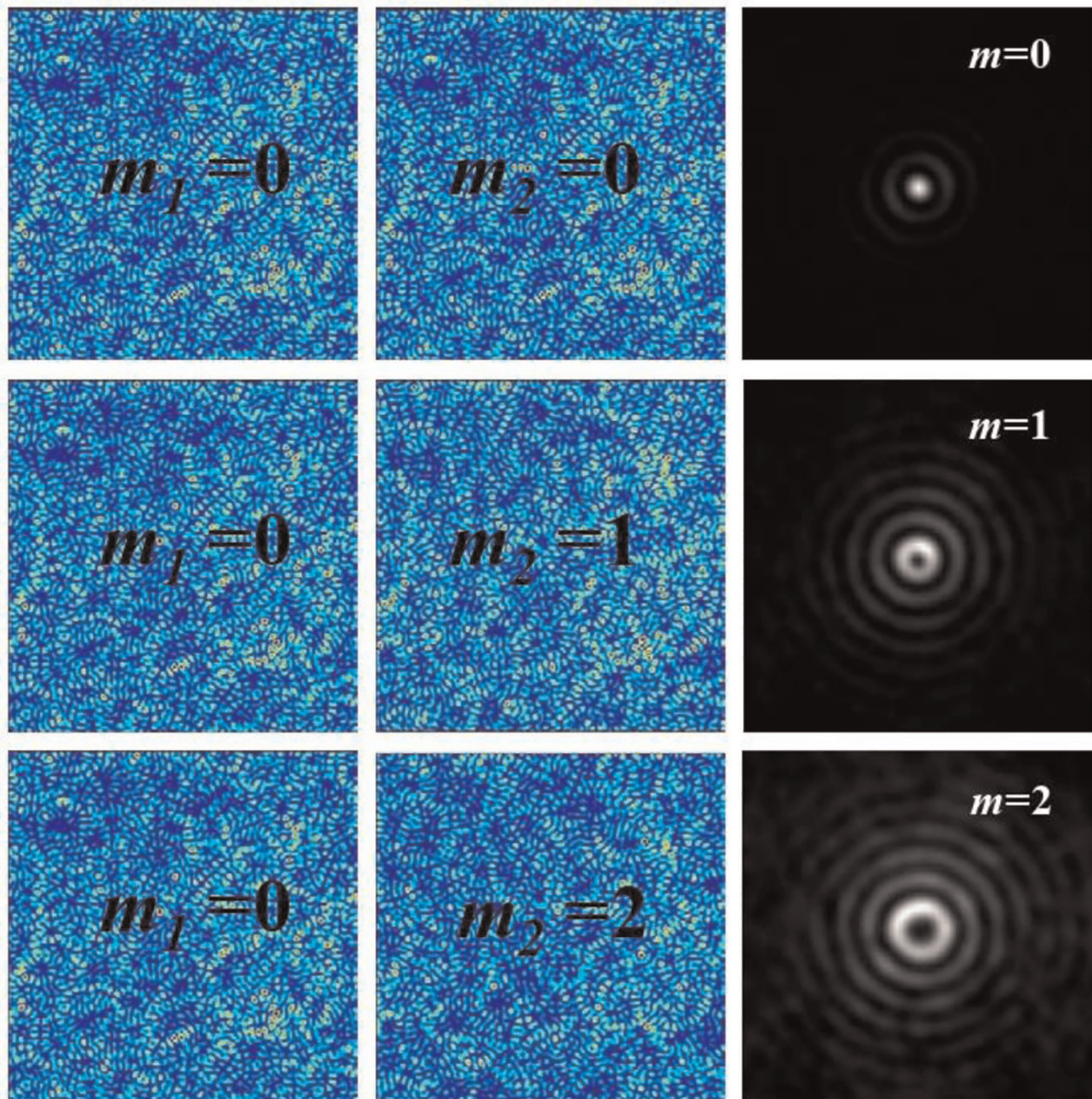


**Figure 12.** The recorded speckle patterns and the corresponding cross-correlation functions, Bessel coherence functions (here  $m = m_2 - m_1$ ).

From Eq. (43), we analyze the size of the speckles under the condition  $m_1=m_2$ , i.e. by considering the width of the autocorrelation function. The speckle size is defined as the spatial length up to which the correlations exist in the field [103, 104]. From Eq. (44), the first zero of zeroth-order Bessel function  $J_0(x) = 0$  can happen at  $x = 2.4$ , and the correlation length or speckle size can be obtained as:

$$\Delta r = \frac{xz}{k\rho_0} = \frac{2.4z}{k\rho_0} \quad (45)$$

It is clear from the aforementioned equation is that the size of near-field speckles varies linearly with propagation distance  $z$ , independent of order  $m$  and inversely proportional to the ring radius  $\rho_0$ . We have observed that the speckle size and distribution are independent of the order, and they vary with propagation distance. The recorded speckles have been shown in **Figure 13**, and the linear variation of speckle size with propagation distance has been verified in **Figure 14**.

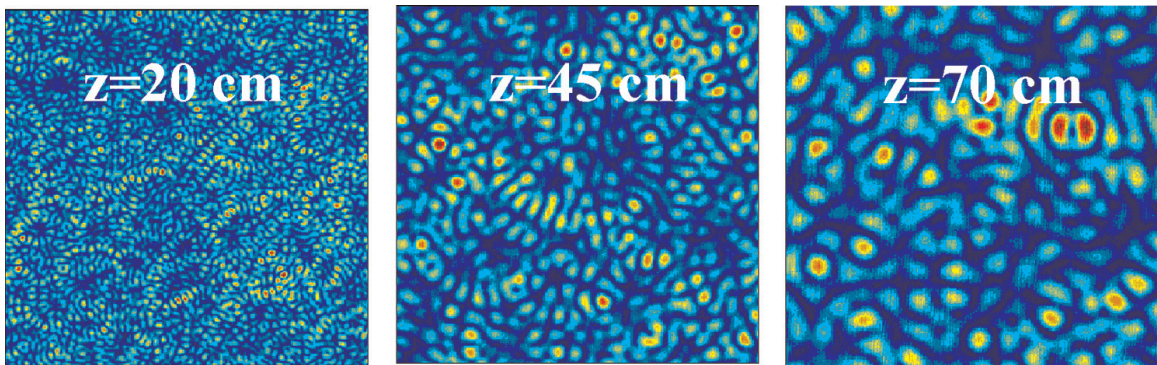


**Figure 13.**  
 The speckle patterns obtained by the scattering of POV beam of order  $m = 0$  at different propagation distances  $z = 20$  cm,  $z = 45$  cm, and  $z = 70$  cm in the near field.

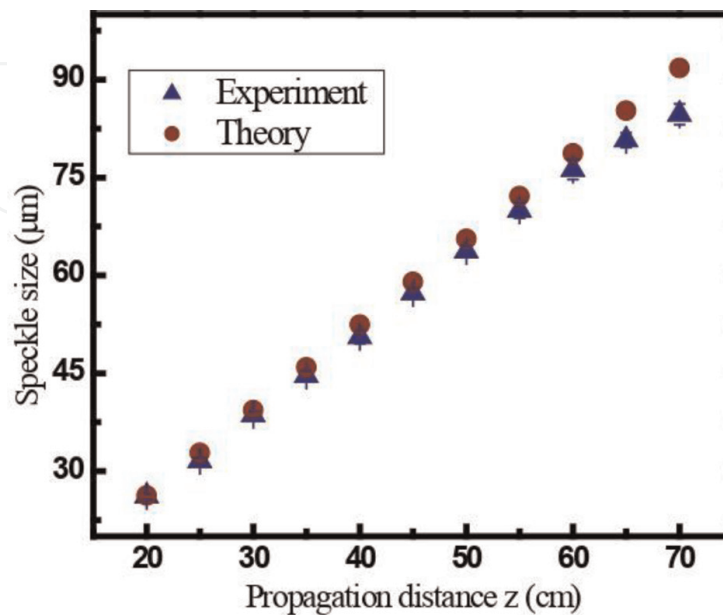


**Figure 14.**  
 Experimental (blue) and theoretical (red) results for the variation of near-field or diverging speckle size with propagation distance.



Further, we consider the Fourier transform of near-field speckles that produce the spatially invariant optical random fields. The Fourier transform can be realized with the help of a simple convex lens (here, we consider its focal length as  $f_2$ ). The far-field autocorrelation function  $\Gamma_{12}'(\Delta r')$  of scattered POV beams is given by [89]:

$$\Gamma_{12}'(\Delta r') = \frac{1}{\lambda^2 f_2^2} \iint |U_1(\rho, \theta)|^2 e^{\frac{-ik}{f_2}(\rho \Delta r' \cos(\varphi_{s1} - \theta))} \rho d\rho d\theta \quad (46)$$

Substituting Eq. (25) in Eq. (46) and following the same procedure, we get

$$\Gamma_{12}'(\Delta r') = \frac{2\pi\rho_0}{\lambda^2 f_2^2} J_0\left(\frac{k\rho_0}{f_2} \Delta r'\right) \quad (47)$$

From the aforementioned equation, one can easily observe that the correlation function is independent of order  $m$  as well as propagation distance  $z$ . As compared to the near-field diffraction, the spatial coherence function does not increase anymore with the propagation which can be utilized for communication and encryption applications.

From Eq. (47), we get the size of non-diffracting random fields as:

$$\Delta r' = \frac{xf_2}{k\rho_0} = \frac{2.4f_2}{k\rho_0} \quad (48)$$

The speckle size is independent of propagation distance  $z$  and directly proportional to focal length  $f_2$  and inversely proportional to ring radius  $\rho_0$ . We can control the size by just varying the focal length and ring radius that can be controlled by axicon parameter [103].

**Figure 15** shows the speckle patterns recorded for different propagation distances and clear that are independent of propagation distances. **Figure 16** shows the variation of speckle for order 2 with propagation distance for different axicon parameters as mentioned. The size of the speckles decreases with the increase in axicon parameter which we attribute to the increase in area of illumination on the GGP. It is also shown that the speckle size is independent of the order.

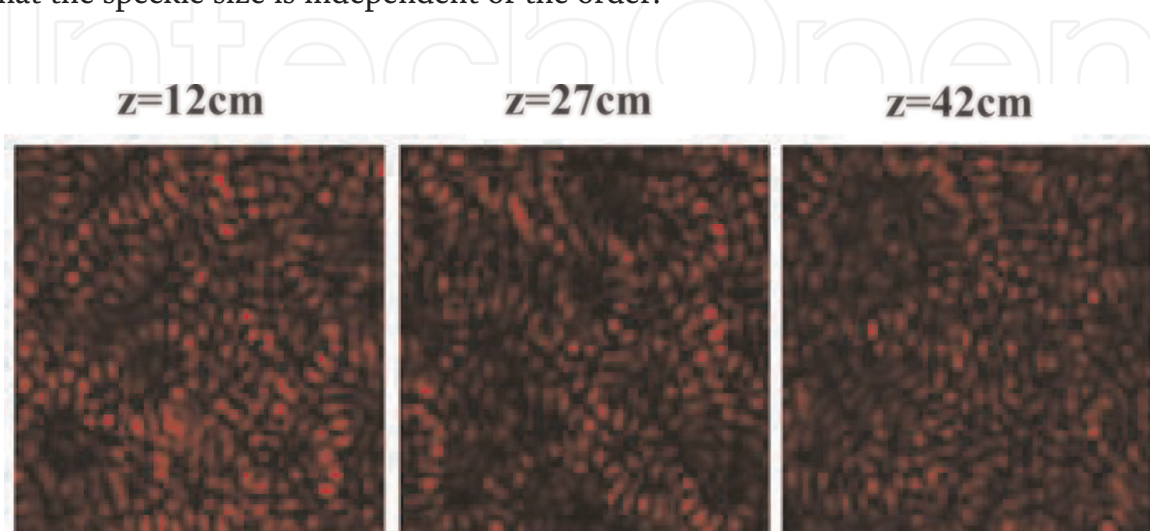


**Figure 15.**  
The speckle patterns obtained by the scattering of POV beam of order  $m = 0$  at different propagation distances in the far field.

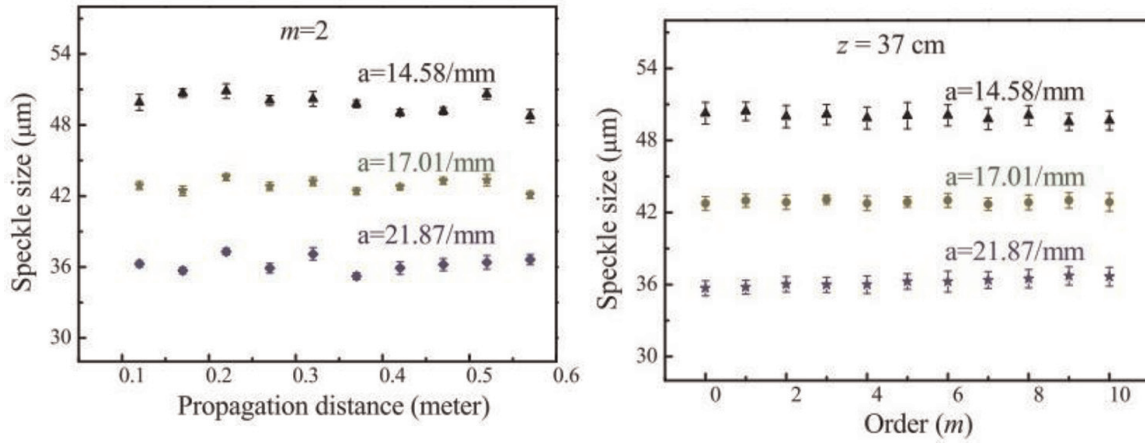


**Figure 16.**  
 The variation of speckle size with the propagation distance (left) and order (right) for different axicon parameters.

#### 4. Physical unclonable functions using the correlations of scattered POV beams

Nowadays, securing private data, i.e. authenticating the authorized users to access the sensitive (personal) information, becomes mandatory. In the cryptographic algorithms, information that needs to be sent from a sender end is encrypted (i.e. input data are converted into an unreadable format) using secret keys. At the receiver end, by appropriately using the keys, encoded information can be retrieved (without loss), and this process is known as decryption. It is known that, depends on the cryptographic algorithm used, the keys for both the encryption and decryption process can be same or different [58, 105, 106]. Due to this reason, cryptographic algorithms are widely used in various fields, such as banking, healthcare, social medias, emails, and military communication, to name a few. However, recent developments in high-performance computers increased the vulnerability of cryptographic techniques for a number of different reasons [106]. To prevent from these attacks, a physical one-way function has been introduced in cryptographic systems which can be (physically) realized using the scattering of light beams [107]. These functions are, in general, known as physical unclonable functions (PUFs) and can be embedded into any optical systems for data authentication as this involves a scattering of light beams which results a random output, i.e. speckles [108]. Some of the advantages of PUF include (i) low cost (ii) high output complexity (iii) difficult to replicate, and (iv) high security against attacks [76, 109, 110]. Therefore, in this work, for the first time, we demonstrate an encryption system (i.e. linear canonical transform-based double random phase encoding (LCT-DRPE)) using PUFs that are generated by taking a correlation function between two speckle patterns obtained after scattering the POV beams through a ground glass plate. We wish to take the extra advantage of order-dependent correlation functions generated by the scattering of POV beams for producing the keys for encryption. Here, one should note that the speckle size and their distribution are order-independent, but the correlation between them is order-dependent [94]. We briefly describe the usage of the correlation functions as keys for encryption along with the decryption process as follows:

The LCT is a three-parameter class of linear integral transform and defined as [111]:



$$\Psi_{\alpha,\beta,\gamma}\{f(x, y)\} = C_1 \int_{-\infty}^{\infty} \int_{-\infty}^{\infty} f(x, y) \exp \{i\pi [\alpha(x^2 + y^2) - 2\beta(ux + vy) + \gamma(u^2 + v^2)]\} dx dy \quad (49)$$

where  $\alpha, \beta, \gamma$  are the real-valued parameters that are independent of the coordinates that are applied symmetrically in both horizontally ( $x$ ) and ( $y$ ), i.e. 2D separable LCT. The encrypted (output) image  $E(\omega, \varphi)$  can be expressed as [112, 113]:

$$E(\omega, \varphi) = LCT\{LCT\{f(x, y) \times O_1(x, y)\} \times O_2(x, y)\} \quad (50)$$

where  $f(x, y)$  is the 2D input image,  $O_1(x, y)$  and  $O_2(x, y)$  are two random phase masks (RPMs) considered as secret keys which are generated using a correlation function obtained from two scattered POV light beams, i.e. speckles. The schematic for LCT-DRPE is shown in **Figure 17**.

The resultant encrypted image resembles a white noise, i.e. speckle image. Therefore, it does not reveal any of the input information. It is therefore possible to reverse this process called decryption and get the original image back without loss. This process is given mathematically as:

$$f(x, y) = ILCT\{ILCT\{E(\omega, \varphi)\} \times O_2^*(x, y)\} \times O_1^*(x, y) \quad (51)$$

where ILCT refers to inverse linear canonical transform and \* denotes the complex conjugate operation. The LCT parameters alpha, beta, and gamma are set as 10,100,1, respectively.

**Figure 18a** shows the input image (i.e. reconstructed hologram of a 3D object) [113, 114], and **Figure 18b** is the amplitude of the complex encrypted image, and information contained in it is very difficult to be observed. **Figure 18c** shows the decrypted image using appropriate secret keys. The decrypted image quality is the classical mean squared error (MSE) which is calculated between the input image and decrypted image.

In **Figure 19**, changes in the LCT parameter yield the fruitful results, i.e. not able to get proper decrypted images for the corresponding input data.

**Encryption using Fourier domain:** This is the one of the methods that allows to encode a primary image into a stationary white noise. We demonstrate how

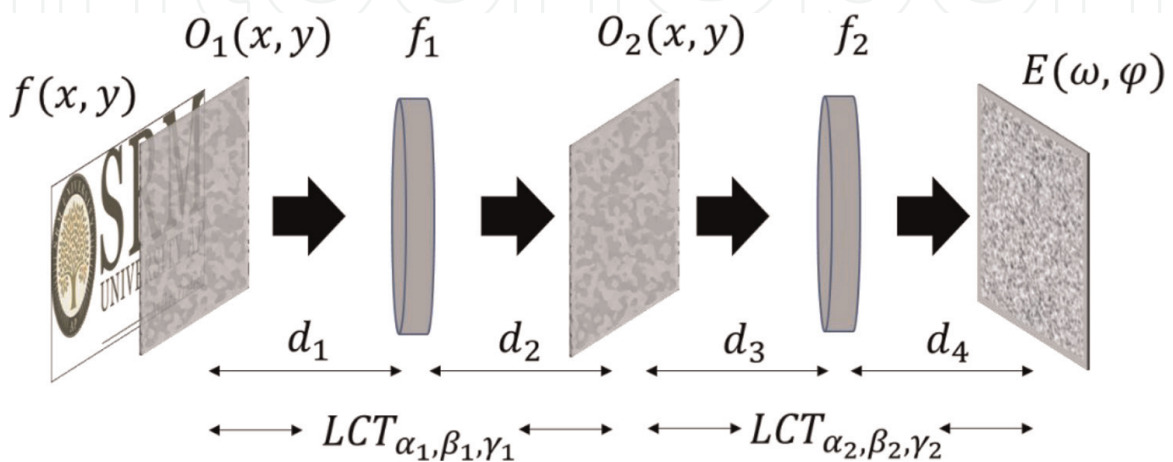


**Figure 17.**  
The schematic for LCT-based DRPE system.

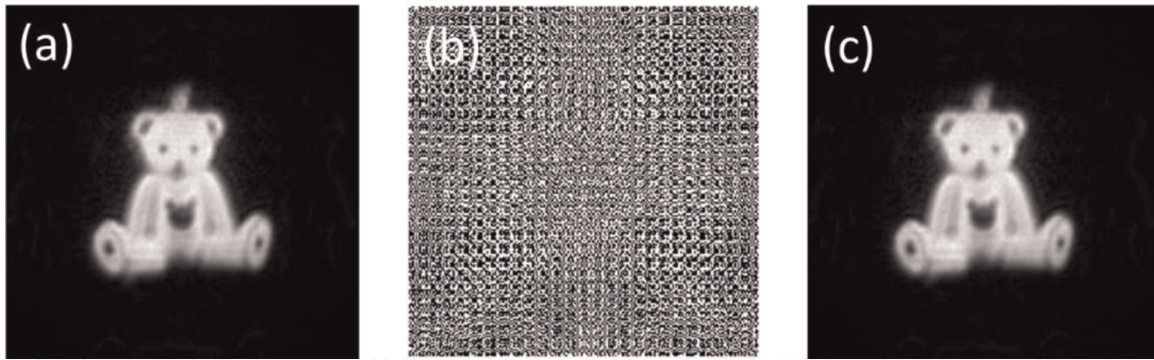


**Figure 18.** Simulation results: (a) input grayscale image, (b) encrypted image, and (c) decrypted image (MSE =  $1.3685e-27$ ).

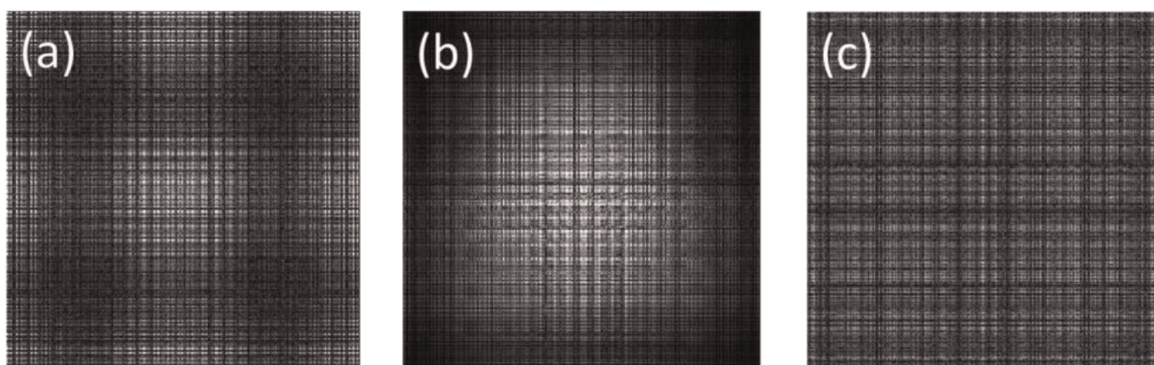


**Figure 19.** Decryption with wrong LCT parameters: (a) alpha is wrong, (b) beta is wrong, and (c) gamma is wrong.

straightforward and reliable it is to rebuild the original image using the encoded image [115]. In fact, it is critical to have the ability to encrypt data in a way that makes it challenging to decode without a key yet simple to do so with a key but easy if one knows that key [116]. Let us consider the input signal to be encoded is a face Images, that is, since the image is a positive function and is two-dimensional, it is well known that it is possible to reconstruct an image from its Fourier magnitude [91, 117, 118]. The encoded image can be expressed as:

$$\psi(x) = \{f(x) \exp(i2\pi n(x))\} * h(x) \quad (52)$$

where  $f(x)$  is the input function and  $\exp(i2\pi n(x))$  is the random phase mask. Then, we convolve this image by the impulse response  $h(x)$  is the Fourier transform of the  $\exp(i2\pi b(\nu))$ . (**Figure 20**)

The encrypted image  $\psi(x)$  is optically Fourier-transformed and multiplied by the phase mask  $\exp(-i2\pi b(\nu))$  and then inverse Fourier-transformed to produce decrypted image. The decrypted image is expected for the input image with the addition of some noise  $u(x)$ .

## 5. Conclusion

In conclusion, we have briefly explained about the correlations present in scattered phase singular beams and their applications toward communication and encryption.

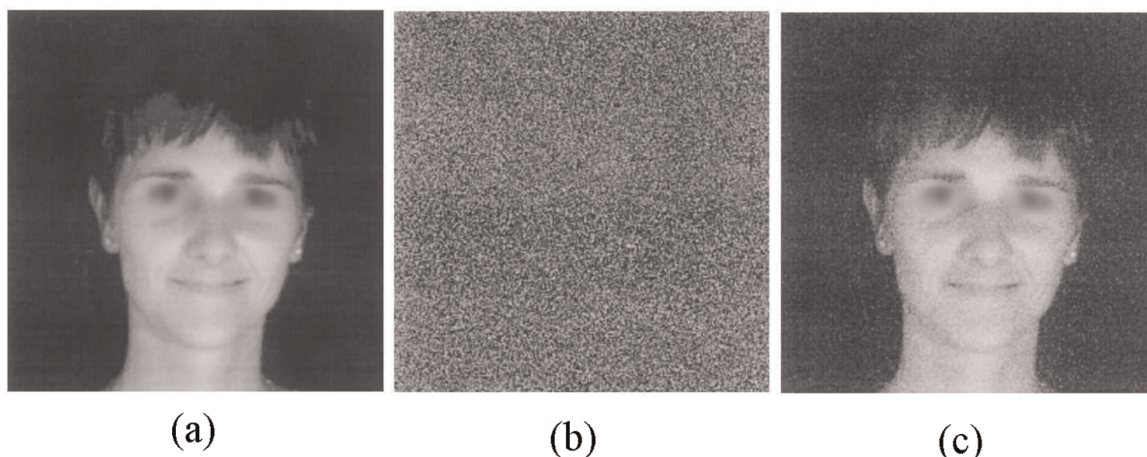


**Figure 20.**

*Simulation results: (a) input grayscale image, (b) encrypted image, and (c) decrypted image.*

We have shown that the number of dark rings present in the autocorrelation function of speckles provides the information about the incident spatial mode, and one can utilize these results in free-space optical communication. Further we have utilized, the cross-correlations present in speckle patterns corresponding to vortices of different orders for generating the coherence vortices. We have discussed the geometry of coherence vortices along with their propagation characteristics. We further discussed about the correlations present in the scattered POV beams which produce the order-independent speckle patterns. Finally, we utilized these cross-correlation functions for encryption applications and discussed in detail.

## Author details


Patnala Vanitha<sup>1</sup>, Gangi Reddy Salla<sup>1\*</sup> and Ravindra Pratap Singh<sup>2</sup>

1 Department of Physics, SRM University-AP, Amaravati, India

2 Physical Research Laboratory, Ahmedabad, India

\*Address all correspondence to: gangireddy.s@srmmap.edu.in

## IntechOpen

© 2022 The Author(s). Licensee IntechOpen. This chapter is distributed under the terms of the Creative Commons Attribution License (<http://creativecommons.org/licenses/by/3.0>), which permits unrestricted use, distribution, and reproduction in any medium, provided the original work is properly cited. 



## References

- [1] Wu Y, Xu C, Qiu H, Xu D, Deng D. Guiding the optical vortex along pre-designed parabolic trajectories from circular symmetric Airy-like beams. *Applied Optics*. 2022;**61**(8):1906-1911
- [2] Song D, Wang H, Ma J, Tang L, Zheng X, Hu Y, et al. Synthetic optical vortex beams from the analogous trajectory change of an artificial satellite. *Photonics Research*. 2019;**7**(9):1101-1105
- [3] Rode AV, Desyatnikov AS, Shvedov VG, Krolikowski W, Kivshar YS. Optical guiding of absorbing nanoclusters in air. *Optics Express*. 2009;**17**(7):5743-5757
- [4] Liu F, Zhang Q, Cheng T, Wu X, Wei Y, Zhang Z. Photophoretic trapping of multiple particles in tapered-ring optical field. *Optics Express*. 2014;**22**(19):23716-23723
- [5] Zhao J, Chremmos ID, Song D, Christodoulides DN, Efremidis NK, Chen Z. Curved singular beams for three-dimensional particle manipulation. *Scientific Reports*. 2015;**5**:12086
- [6] Gong L, Lu R-D, Chen Y, Ren Y-X, Fang Z-X. Generation and characterization of a perfect vortex beam with a large topological charge through a digital micromirror device. *Applied Optics*. 2015;**54**(27):8030-8035
- [7] Stoyanov L, Maleshkov G, Stefanov I, Paulus GG, Dreischuh A. Focal beam structuring by triple mixing of optical vortex lattices. *Optical and Quantum Electronics*. 2022;**54**:34
- [8] Mao D, Zheng Y, Zeng C, Lu H, Wang C, Zhang H, et al. Generation of polarization and phase singular beams in fibers and fiber lasers. *Advanced Photonics*. 2021;**5**:014002
- [9] Bhattacharya R. Generation of phase singular optical beams in microstructure optical fibers. *Optics Communications*. 2018;**428**:15-21
- [10] Wang W, Yokozeki T, Ishijima R, Wada A, Miyamoto Y, Takeda M, et al. Optical vortex metrology for nanometric speckle displacement measurement. *Optics Express*. 2006;**14**(1):120-127
- [11] Shen Y, Wang X, Xie Z, Min C, Fu X, Liu Q, et al. Optical vortices 30 years on: OAM manipulation from topological charge to multiple singularities. *Light: Science & Applications*. 2019;**8**:90
- [12] Kovalev AA, Porfirev AP, Kotlyar VV. Asymmetric Gaussian optical vortex. *Optics Letters*. 2017;**42**(1):139-142
- [13] Curtis JE, Grier DG. Structure of optical vortices. *Physical Review Letters*. 2003;**90**(13):133901-133904
- [14] Allen L, Beijersbergen MW, Spreeuw RJC, Woerdman JP. Orbital angular momentum of light and the transformation of Laguerre-Gaussian laser modes. *Physical Review A*. 1992;**45**:8185-8189
- [15] Berry MV. Optical vortices evolving from helicoidal integer and fractional phase steps. *Journal of Optics A: Pure and Applied Optics*. 2004;**6**:259-268
- [16] Franke-Arnold S, Allen L, Padgett M. Advances in optical angular momentum. *Laser And Photonics Reviews*. 2008;**2**(4):299-313
- [17] Wang WB, Gozali R, Nguyen TA, Alfano RR. Propagation and transmission of optical vortex beams through turbid scattering wall with



- orbital angular momentums. Proceedings of SPIE. 2015;**9318**:931805
- [18] Shi L, Lindwasser L, Alfano RR, Gozali R, Wang WB. Deep transmission of Laguerre–Gaussian vortex beams through turbid scattering media. Optics Letters. 2016;**41**(9):2069-2072
- [19] Zhu K, Li S, Tang Y, Yu Y, Tang H. Study on the propagation parameters of Bessel-Gaussian beams carrying optical vortices through atmospheric turbulence. Journal of the Optical Society of America A. 2012;**29**(3):251-257
- [20] Zhou G, Tang H, Zhu K, Zheng X, Li X. Propagation of Bessel-Gaussian beams with optical vortices in turbulent atmosphere. Optics Express. 2008; **16**(26):21315-21320
- [21] Hufnagel F, Sit A, Grenapin F, Bouchard F, Heshami K, Heshami K, et al. Characterization of an underwater channel for quantum communications in the Ottawa River. Optics Express. 2019; **27**(19):26346-26354
- [22] Mobashery A, Parmoon B, Saghafifar H, Karahroudi MK, Moosavi SA. Performance evaluation of perfect optical vortices transmission in an underwater optical communication system. Applied Optics. 2018;**57**(30): 9148-9154
- [23] Singh M, Atieh A, Grover A, Barukab O. Performance analysis of 40 Gb/s free space optics transmission based on orbital angular momentum multiplexed beams. Alexandria Engineering Journal. 2022;**61**(7): 5203-5212
- [24] Li L, Zhang R, Zhao Z, Xie G, Liao P, Pang K, et al. High-capacity free-space optical communications between a ground transmitter and a ground receiver via a UAV using multiplexing of multiple orbital-angular-momentum beams. Scientific Reports. 2017;**7**:17427
- [25] Gibson G, Courtial J, Vasnetsov M, Padgett MJ, Franke-Arnold S, Barnett SM, et al. Free-space information transfer using light beams carrying orbital angular momentum. Optics Express. 2004;**12**(22):5448-5456
- [26] Qu Z, Djordjevic IB. Orbital angular momentum multiplexed free-space optical communication systems based on coded modulation. Applied Sciences. 2018;**8**(12):2179
- [27] Willner AE, Pang K, Song H, Zou K, Zhou H. Orbital angular momentum of light for communications. Applied Physics Reviews. 2021;**8**:041312
- [28] Eyyuboğlu HT. Optical communication system using Gaussian vortex beams. Journal of the Optical Society of America A. 2020;**37**(10): 1531-1538
- [29] Wang J, Liu J, Li S, Zhao Y, Du J, Zhu L. Orbital angular momentum and beyond in free-space optical communications. Nano. 2022;**11**(4): 645-680
- [30] Chen R, Zhou H, Moretti M, Wang X, Li J, Member S. Orbital angular momentum waves: Generation, Detection and Emerging Applications, IEEE Communications Surveys & Tutorials. 2020;**22**(2):840-868
- [31] White AG, Smith CP, Heckenberg NR, McDuff R. Generation of optical phase singularities by computer-generated holograms. Optics Letters. 1992;**17**(3):221-223
- [32] Li S, Wang Z. Generation of optical vortex based on computer-generated holographic gratings by

photolithography. *Applied Physics Letters*. 2013;**103**:141110

[33] Li D, Xuan L, Hu L, Mu Q, Liu Y, Cao Z. Phase-only liquid-crystal spatial light modulator for wave-front correction with high precision. *Optics Express*. 2004;**12**(26):6403-6409

[34] Efron U. *Spatial Light Modulator Technology: Materials, Devices, and Applications*. New York: Marcel Dekker; 1995

[35] Kovalev AA, Moiseev OY, Skidanov RV, Khonina SN, Soifer VA, Kotlyar VV. Simple optical vortices formed by a spiral phase plate. *Journal of Optical Technology*. 2007;**74**(10): 686-693

[36] Khonina SN, Ustinov AV, Logachev VI, Porfirev AP. Properties of vortex light fields generated by generalized spiral phase plates. *Physical Review A*. 2020;**101**:043829

[37] Beijersbergen MW, Allen L, van der Veen HELO, Woerdman JP. Astigmatic laser mode converters and transfer of orbital angular momentum. *Optics Communications*. 1993;**96**(1-3):123-132

[38] Kano K, Kozawa Y, Sato S. Generation of a purely single transverse mode vortex beam from a He-Ne laser cavity with a spot-defect mirror. *International Journal of Optics*. 2012; **2012**:359141

[39] Guo Y, Pu M, Zhao Z, Wang Y, Jin J, Gao P, et al. Merging geometric phase and plasmon retardation phase in continuously shaped metasurfaces for arbitrary orbital angular momentum generation. *ACS Photonics*. 2016;**3**(11): 2022-2029

[40] Liu C. Vortex beam and its application in optical tweezers. *Journal*

*of Physics: Conference Series*. 2020; **1549**:032012

[41] D'Ambrosio V, Nagali E, Walborn SP, Aolita L, Slussarenko S, Marrucci L, et al. Complete experimental toolbox for alignment-free quantum communication. *Nature Communications*. 2012;**3**:961

[42] Yu S, Pang F, Liu H, Li X, Yang J, Wang T. Compositing orbital angular momentum beams in Bi<sub>4</sub>Ge<sub>3</sub>O<sub>12</sub> crystal for magnetic field sensing. *Applied Physics Letters*. 2017;**111**:091107

[43] Nye J, Berry M. Dislocations in wave trains. *Proceedings of the Royal Society A Mathematical Physical and Engineering Sciences*. 1974;**336**(1605): 165-190

[44] Goodman JW. *Speckle Phenomena in Optics: Theory and Applications*. Second Edition. Washington, USA: SPIE Press; 2013

[45] Dainty JC. *Laser Speckle and Related Phenomena*. London: Springer; 1976

[46] Reddy SG, Prabhakar S, Kumar A, Banerji J, Singh RP. Higher order optical vortices and formation of speckles. *Optics Letters*. 2014;**39**(15):4364-4367

[47] Wang W, Hanson SG, Miyamoto Y, Takeda M. Experimental investigation of local properties and statistics of optical vortices in random wave fields. *Physical Review Letters*. 2005;**94**:103902

[48] Vinu RV. Shaping and analysis of laser speckle for imaging applications, 308210515 [Accessed: June 30, 2022]

[49] Hu XB, Dong MX, Zhu ZH, Gao W, Rosales-Guzmán C. Does the structure of light influence the speckle size? *Scientific Reports*. 2020;**10**:199

- [50] Facchin M, Dholakia K, Bruce GD. Wavelength sensitivity of the speckle patterns produced by an integrating sphere. *Journal of Physics: Photonics*. 2021;3:035005
- [51] Wang S, Fan X, Wan Y, Zhang Z, He Z. High-resolution wavemeter using Rayleigh speckle obtained by optical time domain reflectometry. *Optics Letters*. 2020;45(4):799-802
- [52] Bruce GD, Dholakia K, O'Donnell L, Chen M, Facchin M. Femtometer-resolved simultaneous measurement of multiple laser wavelengths in a speckle wavemeter. *Optics Letters*. 2020;45(7):1926-1929
- [53] Gbur G, Visser TD. Phase singularities and coherence vortices in linear optical systems. *Optics Communications*. 2006;259(2):428-435
- [54] Wang W, Duan Z, Hanson SG, Miyamoto Y, Takeda M. Experimental study of coherence vortices: Local properties of phase singularities in a spatial coherence function. *Physical Review Letters*. 2006;96:073902
- [55] Jesus-Silva AJ, Alves CR, Fonseca EJS. Characterizing coherence vortices through geometry. *Optics Letters*. 2015;40(12):2747-2750
- [56] Heeman W, Steenbergen W, van Dam GM, Boerma EC, Heeman W. Clinical applications of laser speckle contrast imaging: A review. *Journal of Biomedical Optics*. 2019;24(8):080901
- [57] Leibov L, Ismagilov A, Zalipaev V, Nasedkin B, Grachev Y, Petrov N, et al. Speckle patterns formed by broadband terahertz radiation and their applications for ghost imaging. *Scientific Reports*. 2021;11:20071
- [58] Stallings W. *Cryptography and Network Security Principles and Practice*. New York: Prentice Hall; 2022
- [59] Muniraj I, Sheridan JT. *Optical Encryption and Decryption*. SPIE Press Book; 2019
- [60] Vanitha P, Manupati B, Reddy SG, Singh RP, Muniraj I, Anamalamudi S. Augmenting data security: Physical Unclonable Functions for digital holography based quadratic phase cryptography. 2022. DOI: 10.21203/rs.3.rs-1509081/v1
- [61] Léger D, Perrin JC. Real-time measurement of surface roughness by correlation of speckle patterns. *Journal of the Optical Society of America*. 1976;66(11):1210-1217
- [62] Chen C, Yang H. Correlation between turbulence-impacted optical signals collected via a pair of adjacent spatial-mode receivers. *Optics Express*. 2020;28(10):14280-14299
- [63] Dong K, Cheng M, Lavery MPJ, Geng S, Wang P, Guo L. Scattering of partially coherent vortex beam by rough surface in atmospheric turbulence. *Optics Express*. 2022;30(3):4165-4178
- [64] Liu X, Liu L, Chen Y, Cai Y. *Partially coherent vortex beam: From theory to experiment, vortex dynamics and optical vortices*. London: Springer; 2017
- [65] Salem M, Shirai T, Dogariu A, Wolf E. Long-distance propagation of partially coherent beams through atmospheric turbulence. *Optics Communications*. 2003;216(4-6):261-265
- [66] Dong M, Yang Y. Coherent vortices properties of partially coherent Elegant Laguerre-Gaussian beams in the free space. *Optics and Photonics Journal*. 2020;10(6):159-166
- [67] Gbur G, Visser TD. Coherence vortices in partially coherent beams.



Optics Communications. 2003;**222**(1-6): 117-125

[68] Yadav BK, Kandpal HC, Joshi S. Experimental observation of the effect of generic singularities in polychromatic dark hollow beams. *Optics Letters*. 2014; **39**(16):4966-4969

[69] Fel'de CV, Wolf E, Bogatyryova GV, Soskin MS, Polyanskii PV, Ponomarenko SA. Partially coherent vortex beams with a separable phase. *Optics Letters*. 2003;**28**(11):878-880

[70] Jesus-Silva AJ, Neto APS, Alves CR, Amaral JP, Neto JGMN. Measuring the topological charge of coherence vortices through the geometry of the far-field cross-correlation function. *Applied Optics*. 2020;**59**(6):1553-1557

[71] Paterson C. Atmospheric turbulence and orbital angular momentum of single photons for optical communication. *Physical Review Letters*. 2005;**94**:153901

[72] Davidson FM, Ricklin JC. Atmospheric turbulence effects on a partially coherent Gaussian beam: Implications for free-space laser communication. *Journal of the Optical Society of America A*. 2002;**19**(9): 1794-1802

[73] Liu X, Peng X, Liu L, Wu G, Zhao C, Wang F, et al. Self-reconstruction of the degree of coherence of a partially coherent vortex beam obstructed by an opaque obstacle. *Applied Physics Letters*. 2017;**110**(18):181104

[74] Wu G, Cai Y. Detection of a semirough target in turbulent atmosphere by a partially coherent beam. *Optics Letters*. 2011;**36**(10): 1939-1941

[75] Kermisch D. Partially coherent image processing by laser scanning.

*Journal of the Optical Society of America*. 1975;**65**(8):887-891

[76] Wang P, Chen F, Li D, Sun S, Huang F, Zhang T, et al. Authentication of optical physical unclonable functions based on single-pixel detection. *Physical Review Applied*. 2021;**16**:054025

[77] Mandel L, Wolf E. *Optical Coherence and Quantum Optics*. New York: Cambridge University Press; 1995

[78] Wolf E, Gbur G, Schouten HF, Visser TD. Phase singularities of the coherence functions in Young's interference pattern. *Optics Letters*. 2003;**28**(12):968-970

[79] Vanitha P, Lal N, Rani A, Das BK, Salla GR, Singh RP. Correlations in scattered perfect optical vortices. *Journal of Optics*. 2021;**23**:095601

[80] Jesus-Silva AJ, Hickmann JM, Fonseca EJS, Allen L, Beijersbergen MW, Spreeuw RJ, et al. Strong correlations between incoherent vortices. *Optics Express*. 2012;**20**(18):19708-19713

[81] Anwar A, Permangatt C, Banerji J, Singh RP, Reddy SG, Prabhakar S. Divergence of optical vortex beams. *Applied Optics*. 2015;**54**(22):6690-6693

[82] Vallone G, Parisi G, Spinello F, Mari E, Tamburini F, Villoresi P. General theorem on the divergence of vortex beams. *Physical Review A*. 2016;**94**: 023802

[83] Mazilu M, Mourka A, Vettenburg T, Wright EM, Dholakia K. Determination of the azimuthal and radial mode indices for light fields possessing orbital angular momentum. *Frontiers in Optics/Laser Science XXVIII*, Paper FW4A.4. 2012

[84] Mazilu M, Mourka A, Vettenburg T, Wright EM, Dholakia K. Simultaneous



determination of the constituent azimuthal and radial mode indices for light fields possessing orbital angular momentum. *Applied Physics Letters*. 2012;**100**(23):231115

[85] Yang Y, Chen M, Mazilu M, Mourka A, Liu YD, Dholakia K. Effect of the radial and azimuthal mode indices of a partially coherent vortex field upon a spatial correlation singularity. *New Journal of Physics*. 2013;**15**:113053

[86] Yang Y, Dong Y, Zhao C, Liu Y, Cai Y, McMorran BJ, et al. Autocorrelation properties of fully coherent beam with and without orbital angular momentum. *Optics Express*. 2014;**22**:2925

[87] Vanitha P, Manupati B, Reddy SG, Annapureddy V, Prabhakar S, Singh RP. Intensity correlations in perturbed optical vortices: Diagnosis of the topological charge. 2022. DOI: 10.48550/arxiv.2206.02365

[88] Peatross J, Ware M. *Physics of light and optics: A free online textbook*. *Frontiers in Optics/ Laser Science XXVI*, Paper JWA64. 2010

[89] Dogariu A, Acevedo CH. Non-evolving spatial coherence function. *Optics Letters*. 2018;**43**(23):5761-5764

[90] Gradshteyn IS, Ryzhik IM. *Table of integrals, series, and products*. Washington, USA: Academic Press; 2014

[91] Goodman JW. *Introduction to Fourier optics*. Colorado, USA: Robert and Company Publishers; 1996

[92] Kumar A, Banerji J, Singh RP, Prabhakar S. Revealing the order of a vortex through its intensity record. *Optics Letters*. 2011;**36**(22):4398-4400

[93] Yue Y, Yan Y, Ahmed N, Yang JY, Zhang L, Ren Y, et al. Mode and propagation effects of optical orbital angular momentum (OAM) modes in a ring fiber. *IEEE Photonics Journal*. 2012;**4**(2):535-543

[94] Ostrovsky AS, Rickenstorff-Parrao C, Arrizón V. Generation of the perfect optical vortex using a liquid-crystal spatial light modulator. *Optics Letters*. 2013;**38**(4):534-536

[95] Anaya Carvajal N, Acevedo CH, Torres Moreno Y. Generation of perfect optical vortices by using a transmission liquid crystal spatial light modulator. *International Journal of Optics*. 2017; **2017**:6852019

[96] Yuan W, Xu Y, Xu Y, Zheng K, Fu S, Fu S, et al. Experimental generation of perfect optical vortices through strongly scattering media. *Optics Letters*. 2021; **46**(17):4156-4159

[97] Kotlyar VV, Kovalev AA, Porfirev AP. Elliptic perfect optical vortices. *Optik*. 2018;**156**:49-59

[98] Chen M, Mazilu M, Arita Y, Wright EM, Dholakia K. Dynamics of microparticles trapped in a perfect vortex beam. *Optics Letters*. 2013; **38**(22):4919-4922

[99] Rusch L, Vaity P. Perfect vortex beam: Fourier transformation of a Bessel beam. *Optics Letters*. 2015;**40**(4): 597-600

[100] Kumar A, Singh RP, Reddy SG, Prabhakar S. Experimental generation of ring-shaped beams with random sources. *Optics Letters*. 2013;**38**(21): 4441-4444

[101] Gori F, Guattari G, Padovani C. Bessel-Gauss beams. *Optics*

Communications. 1987;**64**(6):  
491-495

[102] McLeod JH. The Axicon: A new type of optical element. *Journal of the Optical Society of America*. 1954;**44**(8): 592-597

[103] Reddy SG, Chithrabhanu P, Vaity P, Aadhi A, Prabhakar S, Singh RP. Non-diffracting speckles of a perfect vortex beam. *Journal of Optics*. 2016;**18**: 055602

[104] Vanitha P, Rani A, Annapureddy V, Reddy SG, Singh RP. Diffracting and Non-diffracting random fields. 2021. <https://doi.org/10.48550/arxiv.2111.12388>.

[105] Vaudenay S. *A Classical Introduction to Cryptography*. New York: Springer; 2008

[106] Stallings W. *Cryptography and Network Security Principles and Practice*. New York: Prentice Hall; 2011

[107] Pappu R, Recht B, Taylor J, Gershenfeld N. Physical one-way functions. *Science*. 2002;**297**(5589): 2026-2030

[108] Bohm C, Hofer M, *Physical Unclonable functions in theory and practice*. New York: Springer Publishers; 2013

[109] Chen K, Huang F, Wang P, Wan Y, Li D, Yao Y. Fast random number generator based on optical physical unclonable functions. *Optics Letters*. 2021;**46**(19):4875-4878

[110] Shamsoshoara A, Korenda A, Afghah F, Zeadally S. A survey on physical unclonable function (PUF)-based security solutions for Internet of Things. *Computer Networks*. 2020;**183**: 107593

[111] Lee B-G, Guo C, Muniraj I, Ryle JP, Healy JJ, Sheridan JT, et al. Low photon count based digital holography for quadratic phase cryptography. *Optics Letters*. 2017;**42**(14):2774-2777

[112] Liu S, Guo C, Sheridan JT. A review of optical image encryption techniques. *Optics & Laser Technology*. 2014;**57**: 327-342

[113] Muniraj I, Ryle JP, Healy JJ, Sheridan JT, Wan M, Chen N, et al. Orthographic projection images-based photon-counted integral Fourier holography. *Applied Optics*. 2019; **58**(10):2656-2661

[114] Lam EY, Chen N, Ren Z. High-resolution Fourier hologram synthesis from photographic images through computing the light field. *Applied Optics*. 2016;**55**(7):1751-1756

[115] Javidi B, Refregier P. Optical image encryption based on input plane and Fourier plane random encoding. *Optics Letters*. 1995;**20**(7):767-769

[116] Jumarie G. *Relative Information*. Berlin: Springer-Verlag; 1990

[117] Hayes MH. In: Stark H, editor. *Image Recovery: Theory and Application*. San Diego, CA: Academic; 1987

[118] Dainty JC, Fienup JR. In: Stark H, editor. *Image Recovery: Theory and Application*. San Diego, CA: Academic; 1987